

1 Development of the DRoplet Ice Nuclei Counter Zürich (DRINCZ): 2 Validation and application to field collected snow samples

3 Robert O. David^{1,*}, Maria Cascajo-Castresana^{1,2}, Killian P. Brennan¹, Michael Rösch¹, Nora Els⁴, Julia
4 Werz³, Vera Weichlinger¹, Lin S. Boynton³, Sophie Bogler³, Nadine Borduas-Dedekind^{1,3}, Claudia
5 Marcolli¹, Zamin A. Kanji¹

6 ¹Institute of Atmospheric and Climate Science, ETH Zürich, Zürich, 8092, Switzerland

7 ²CIC nanoGUNE Consolider, Donostia-San Sebastian, E-20018, Spain

8 ³Institute for Biogeochemistry and Pollutant Dynamics, ETH Zürich, Zürich, 8092, Switzerland

9 ⁴Institute of Ecology, University of Innsbruck, Innsbruck, 6020, Austria

10 ^{*}Now at Department of Geosciences, University of Oslo, Oslo, 0315, Norway

11
12 *Correspondence to:* Robert O. David (r.o.david@geo.uio.no) and Zamin A. Kanji (zamin.kanji@env.ethz.ch)

13 **Abstract.** Ice formation in the atmosphere is important for regulating cloud lifetime, Earth's radiative balance and initiating
14 precipitation. Due to the difference in the saturation vapor pressure over ice and water, in mixed-phase clouds (MPCs), ice
15 will grow at the expense of supercooled cloud droplets. As such, MPCs, which contain both supercooled liquid and ice, are
16 particularly susceptible to ice formation. However, measuring and quantifying the concentration of ice nucleating particles
17 (INPs) responsible for ice formation at temperatures associated with MPCs is challenging due to their very low concentrations
18 in the atmosphere (~ 1 in 10^5 at -30 °C). Atmospheric INP concentrations vary over several orders of magnitude at a single
19 temperature and strongly increase as temperature approaches the homogeneous freezing threshold of water. To further quantify
20 the INP concentration in nature and perform systematic laboratory studies to increase the understanding of the properties
21 responsible for ice nucleation, a new drop freezing instrument, the DRoplet Ice Nuclei Counter Zurich (DRINCZ) is developed.
22 The instrument is based on the design of previous drop freezing assays and uses a USB camera to automatically detect freezing
23 in a 96-well tray cooled in an ethanol chilled bath with a user friendly and fully automated analysis procedure. Based on an in-
24 depth characterization of DRINCZ, we develop a new method for quantifying and correcting temperature biases across drop
25 freezing assays. DRINCZ is further validated performing NX-illite experiments, which compare well with the literature. The
26 temperature uncertainty in DRINCZ was determined to be ± 0.9 °C. Furthermore, we demonstrate the applicability of DRINCZ
27 by measuring and analyzing field collected snow samples during an evolving synoptic situation in the Austrian Alps. The field
28 samples fall within previously observed ranges for cumulative INP concentrations and show a dependence on air mass origin
29 and upstream precipitation amount.

30 **1 Introduction**

31 In the atmosphere, ice plays an important role in initiating precipitation and affects the radiative properties of clouds. As much
32 as 80% of land falling precipitation initiates through the ice phase (Mülmenstädt et al., 2015), making it essential to understand
33 the pathways for ice formation in the atmosphere. The ratio of cloud droplets to ice crystals in a mixed-phase cloud (MPC)
34 alters the radiative properties of the cloud and its lifetime (Lohmann and Feichter, 2005; Matus and L'Ecuyer, 2017; Tan et
35 al., 2016). This ratio is important for future climate projections as warmer temperatures will lead to a decrease in ice content,
36 ultimately increasing cloud lifetime and cloud albedo (Tan et al., 2016). Additionally, ice formation at temperatures above
37 $-38\text{ }^{\circ}\text{C}$ in the atmosphere occurs primarily in MPCs through the freezing of cloud droplets (Ansmann et al., 2009; Boer et al.,
38 2011; Westbrook and Illingworth, 2011). Therefore, understanding ice formation in conditions associated with MPCs is of the
39 utmost importance.

40
41 When an ice nucleating particle (INP) gets immersed in a cloud droplet either by acting as cloud condensation nucleus or
42 through scavenging by a cloud droplet, the INP can induce ice formation by reducing the energy barrier associated with the
43 formation of an ice germ and thus freeze at warmer temperatures than homogeneous freezing (Vali et al., 2015). To reproduce
44 the immersion freezing pathway in the laboratory, several methods are used. Single particle methods, such as continuous flow
45 diffusion chambers (Rogers, 1988; Stetzer et al., 2008) operated at water supersaturated conditions (DeMott et al., 2015, 2017;
46 Hiranuma et al., 2015), or with extended chambers that activate individual particles into cloud droplets before exposing them
47 to supercooled conditions (Burkert-Kohn et al., 2017; Kohn et al., 2016; Lüönd et al., 2010) allow for the quantification of the
48 number concentration of INPs as a function temperature. Larger laboratory based single particle methods for examining INPs
49 in the immersion mode include expansion chambers where cloud droplets are first formed by adiabatic cooling due to the
50 expansion of an air volume (Niemand et al., 2012) or experiments where droplets are initially activated and then subsequently
51 cooled as they travel through a laminar flow tube (Hartmann et al., 2011). Aerosols introduced into such systems by dry
52 dispersion or atomization of suspensions and solutions allow for a range of particulates to be examined. However, the single
53 particle methods have detection limitations due to the background ice crystal concentration of the chamber and the optical
54 methods for discriminating between ice and water. Due to the rarity of INPs at MPC conditions, single particle methods are
55 typically unable to quantify INP concentrations within natural ambient samples at temperatures higher than approximately -
56 $22\text{ }^{\circ}\text{C}$ in remote regions without the use of concentrators (Cziczo et al., 2017).

57
58 In contrast bulk methods such as, drop freezing assays (Hill et al., 2014; Stopelli et al., 2014; Vali, 1971), differential scanning
59 calorimetry (Kaufmann et al., 2016; Pinti et al., 2012) and microfluidic devices (Reicher et al., 2018; Riechers et al., 2013;
60 Stan et al., 2009; Tarn et al., 2018) immerse the samples in water and can be used to detect lower atmospheric INP
61 concentrations. The majority of atmospheric INP concentrations at temperatures above $-15\text{ }^{\circ}\text{C}$ has been quantified using drop
62 freezing assays. To retrieve the concentrations of INP from such bulk suspensions, Vali, (1971; 2019) showed that by dividing

63 a sample into several aliquots, it is possible to calculate the number of INPs present in the sample as a function of temperature.
64 The probability for more than one INP in an aliquot that freezes at the same temperature can be predicted using Poisson's Law
65 (Vali, 1971). Following Vali (1971), the cumulative number of INPs in a given sample for each temperature can be calculated
66 as:

$$67 \quad INP(T) = \frac{-\ln(1-FF(T))}{V_a} \quad (1)$$

68 where $FF(T)$ is the fraction of frozen aliquots at a given temperature, T , and V_a is the volume of an aliquot. As can be seen in
69 Eq. 1, the only way to extend the range of measureable INPs across temperature scales is to change V_a . Due to instrumental
70 limitations, it is often difficult to change V_a by significantly enough values for a change in $INP(T)$ within a single instrumental
71 setup. Rather it is easier to dilute the initial sample thereby reducing the number of INPs in each aliquot. Alternatively, to
72 explore freezing towards warmer temperatures, field samples (e.g. rain or snow samples) can be concentrated by evaporating
73 a part of the water. To account for dilution, Eq. 1 can be rewritten as:

$$74 \quad INP(T) = \frac{-\ln(1-FF(T))DF}{V_a} \quad (2)$$

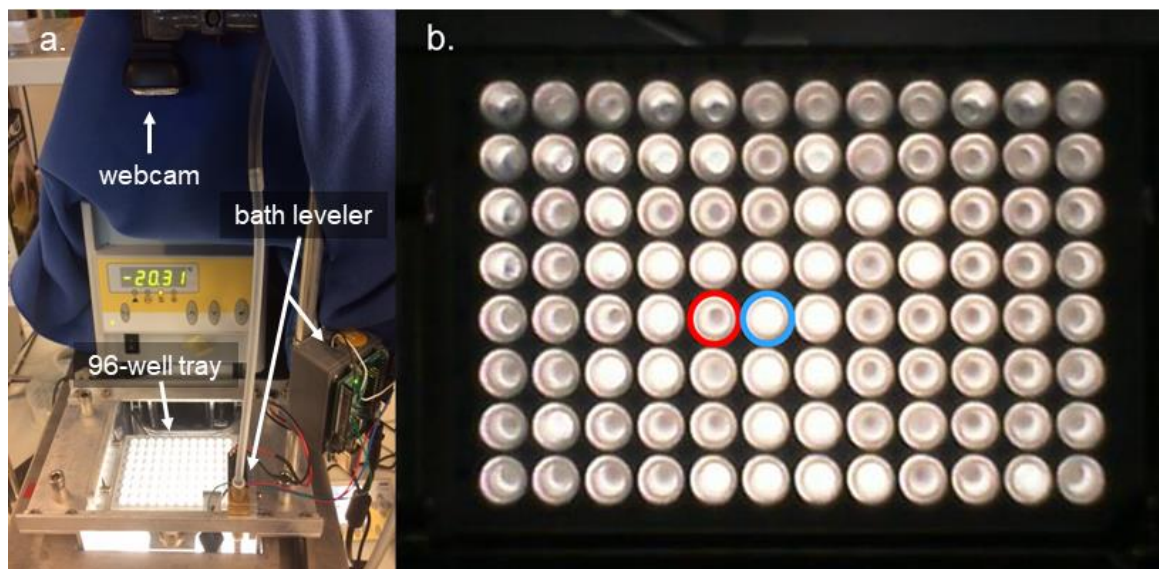
75 where DF is the dilution factor of the initial sample. However, in some cases dilution alone cannot be used to observe the total
76 number of $INP(T)$ due to the presence of impurities that act as INPs in the water used for dilution (Polen et al., 2018).
77 Therefore, it is necessary to use different bulk techniques that measure aliquots with volumes that span several orders of
78 magnitude, typically microliter to picoliter volumes (Harrison et al., 2018; Hill et al., 2014; Murray et al., 2010; Whale et al.,
79 2015).

80
81 Studies have investigated the concentrations of INPs in the atmosphere over the last 50 years and show that the concentration
82 in the atmosphere spans several orders of magnitude (Fletcher, 1962; Kanji et al., 2017; Petters and Wright, 2015; Welti et al.,
83 2018). Some of the original studies investigated the INP concentrations in melted hail and snow samples e.g. (Vali, 1971).
84 Since then, studies have diversified to sampling INPs directly from the air (Boose et al., 2016b; Creamean et al., 2013; DeMott
85 et al., 2003; Lacher et al., 2017; Richardson et al., 2007; Welti et al., 2018), from precipitation (Christner et al., 2008; Hill et
86 al., 2014; Petters and Wright, 2015; Stopelli et al., 2015) and investigated potential types of INPs in the laboratory from
87 commercial and naturally occurring samples as well as field collected samples (Atkinson et al., 2013; Boose et al., 2016a;
88 Broadley et al., 2012; Felgitsch et al., 2018; Hill et al., 2014; Hiranuma et al., 2015, 2019; Kaufmann et al., 2016; Murray et
89 al., 2012; Pummer et al., 2012; Wex et al., 2015). Yet the atmospheric variability in INP concentrations remains unresolved
90 (Hoose and Möhler, 2012; Kanji et al., 2017; Petters and Wright, 2015; Welti et al., 2018). In order to further quantify the
91 variability of ambient INP concentration relevant for ice formation in MPCs and increase the understanding of the ice
92 nucleation ability of laboratory and field collected samples, we developed and characterized the DRoplet Ice Nuclei Counter
93 Zurich (DRINCZ). DRINCZ is a drop freezing instrument to investigate ice nucleation at temperature conditions between -25
94 °C and 0 °C, representative for MPCs. Furthermore, DRINCZ complements and extends the INP concentration measurement
95 capabilities of the single particle and bulk methods employed at ETH Zürich e.g. (Kohn et al., 2016; Lacher et al., 2017; Lüönd

96 et al., 2010; Marcolli et al., 2007; Stetzer et al., 2008). The automation of DRINCZ and its portable design allows for the
97 acquisition of INP data in the field and laboratory, ultimately increasing the attainable information about the global distribution
98 of INPs.

99 2 Instrument Design

100 DRINCZ is based on the design of Stopelli et al. (2014) and Hill et al. (2014), which was initially suggested by (Vali and
101 Upper, 1995). It consists of a temperature controlled ethanol bath (Lauda ProLine RP 845, Lauda-Königshofen, Germany), a
102 home-built LED light consisting of several LED light strips enclosed in an ethanol proof housing, a home-built 96-well tray
103 holder and camera mount, a webcam (Microsoft Lifecam HD-3000) and a custom designed bath leveler, composed of a bath
104 level sensor and valve (see Section 2.2) (Fig. 1a). The working principle is similar to that of Stopelli et al. (2014), in that a
105 USB camera detects the light transmission through aliquots of sample. In DRINCZ, the aliquots are typically 50 μL and
106 dispensed into a 96-well polypropylene tray (732-2386, VWR, USA). To avoid contamination, the top of the 96-well tray is
107 sealed with a transparent non-permeable foil (Axgen, Platemax CycloSeal Sealing Film, PCR-TS). The well tray is placed in
108 the tray holder (Fig. A1) and left to rest for 1 min at 0 $^{\circ}\text{C}$ before the cooling ramp is started. The webcam is programmed to
109 take a picture every 15 seconds, which corresponds to a picture taken approximately every 0.25 $^{\circ}\text{C}$ decrease when the bath is
110 cooled at a rate of 1 $^{\circ}\text{C min}^{-1}$. Moreover, both the picture frequency and cooling rate are adjustable. Upon freezing, the light
111 transmission through an individual well decreases (red circled well in Fig. 1b) due to the polycrystallinity of the ice frozen in
112 the wells.



113
114 **Figure 1: (a) Picture of DRINCZ. (b) Change in light transmission through the wells during an experiment with an example of an**
115 **unfrozen (blue circle) and frozen (red circle) well.**

116 The cooling cycle of the ethanol-based Lauda bath is controlled using LabVIEW® and the bath temperature is written to a text
117 file that is then read in by MATLAB® during the analysis. In addition, MATLAB® is also used to take and save the pictures
118 from the webcam. Both the LabVIEW® generated text file and pictures from the experiment are stored in the same folder for
119 data handling. A suite of MATLAB® functions have been written to automatically analyze and store the data from each
120 experiment, allowing for minimal user input (details of the code are provided in Appendix A) and rapid experiment throughput
121 of approximately 30 minutes per experiment and 2 minutes to process the data for frozen fraction as a function of temperature.

122 **2.1 Detection Method**

123 Similar to Stopelli et al, (2014), the ice nucleation detection in DRINCZ is achieved by the attenuation of visible radiation due
124 to a frozen well compared to transmission through a supercooled well. The images are analyzed by first detecting the pixels
125 that correspond to each well of the 96-well tray and then calculating the change of the average well brightness during an
126 experiment between one picture and the next. The well detection method is described in the following subsection, followed by
127 the technique used to detect well freezing.

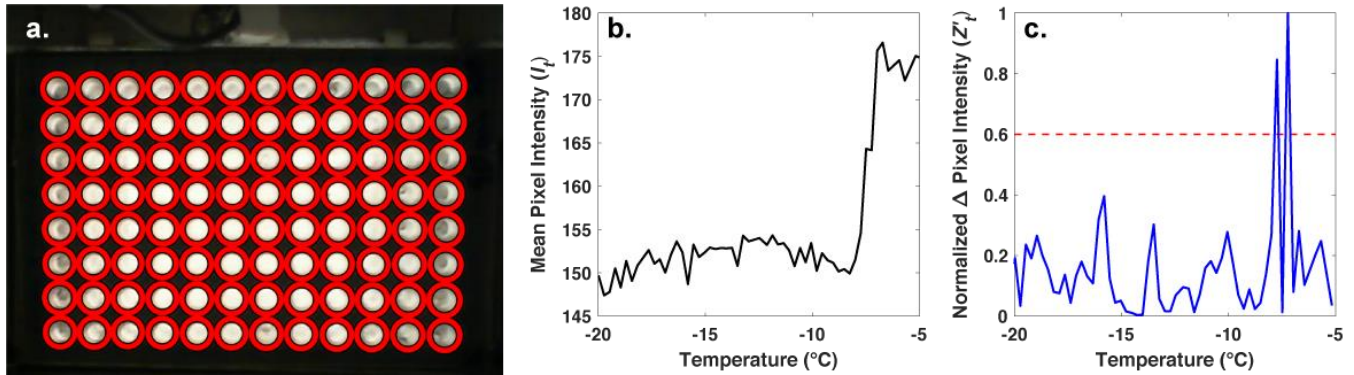
128 **2.1.1 Circular Hough Transform for Well Detection**

129 A fixed 96-well tray holder with an integrated webcam mount reduces variations in setting up the experiment. Nevertheless,
130 small changes in the location of the webcam due to mechanical shock during transport or testing, can produce misidentified
131 wells when algorithms rely on fixed well locations. Therefore, a freezing detection algorithm was developed to avoid errors
132 arising from small changes in the location of the wells. To optimize contrast, the PCR tray holder was constructed out of
133 aluminum so that light transmission only occurs through the wells (see Fig. A1). The high contrast between the illuminated
134 wells and dark tray holder allows for the automatic detection of the wells using a Circular Hough Transform (CHT) (e.g.
135 Atherton and Kerbyson, 1999). The CHT first identifies pixels along regions of large gradients in brightness, to identify the
136 pixels at the edge of the well. To determine the center of each well, the algorithm draws circles of varying diameter (ranging
137 between 7 and 15 pixels in radius, which corresponds to the previously observed diameters of a well in terms of pixel number)
138 around these edge pixels and classifies the pixel intersecting the largest number of circles as the well center. The radius of the
139 well is then given as the radius of the circles that led to the highest number of intersections. The pixels within a well are then
140 identified as the ones encompassed by a circle drawn from a well center with the calculated radius as denoted by the red circles
141 in Fig. 2a. Since the CHT identifies the well center locations in random order, they must be sorted based on their x and y
142 coordinates using a pixel scale for spatial biases or refreezing results to be analyzed. The wells are sorted based on their center
143 locations using the following equation:

$$144 \quad C_i = \frac{y_i}{D} L_x + x_i \quad (3)$$

145 where C_i is the value of the well center based on its pixel location in y and x coordinates, y_i and x_i , respectively, with the
146 origin taken as the pixel in the upper left hand corner of the image. L_x is the pixel number across the well array in the x

147 coordinate and D is the diameter (pixel number) of the wells. All the C_i values are then sorted to ensure that the wells are
 148 identified based on their location independent of the experiment.



149
 150 **Figure 2: (a) Automatic detection of the wells (red circles) using a CHT. (b) Light intensity or I_t of a single well as a function of**
 151 **temperature as observed by the webcam and (c) the normalized change in pixel intensity, Z'_t , for the same well as in b between**
 152 **subsequent pictures taken during an experiment, as a function of temperature. The most intense peak corresponds to the ice**
 153 **nucleation temperature and the second most intense peak is due to the slow freezing of the solution after nucleation. The dashed red**
 154 **line represents the 0.6 threshold required for a well to be classified as frozen.**

155

156 2.1.2 Freezing Detection

157 With the well locations identified, the intensity values of the pixels within each well are averaged for each image recorded
 158 during an experiment (I_t). The change in I_t between subsequent images is used to identify the image where freezing occurred
 159 and the corresponding temperature (Fig. 2b). However, due to the slow freezing process which is limited by the latent heat
 160 release, the light transmission of a well continuously changes until the water is completely frozen as can be seen as two large
 161 peaks in Fig. 2c. To correctly identify the point in time when ice nucleation and not just freezing within the well occurs, the
 162 maximum change in I_t between subsequent images is normalized to 1 using the following procedure:

163 First, the Z-score (Z_t) of I_t is taken to level out differences in illumination within the 96-well tray:

$$164 Z_t = \frac{I_t - \mu}{\sigma} \quad (4)$$

165 where μ and σ are the mean and standard deviation of I_t for all images of a well, respectively. The absolute value of the time
 166 derivative or the change in Z_t between subsequent images (dt) is given as:

$$167 Z'_t = \left| \frac{Z_t}{dt} \right| \quad (5)$$

168 Z'_t is then normalized to 1 by dividing by the maximum Z'_t of the well. The normalization ensures that a fixed threshold for the
 169 identification of ice nucleation can be used rather than relying on a fixed change in light transmission through the well as done
 170 by other drop freezing setups (Beall et al., 2017). This ensures that the initial freezing detection is independent of the absolute
 171 change in light transmission through a well. Based on validation experiments, a threshold value of $0.6 \left(\frac{Z'_t}{\max(Z'_t)} \geq 0.6 \right)$ was

172 found to be best for detecting the initial freezing and to avoid assigning subsequent changes in transparency as a nucleation
173 event due to slow freezing.

174 **2.2 Bath Leveler**

175 Due to the thermal contraction of the ethanol in the chilled bath between 0 and -30 °C, the ethanol level within the bath
176 decreases during an experiment, affecting the immersion level of the wells and thus the thermal contact. It has been shown that
177 large vertical gradients of up to 1.8 °C can exist between the bottom of a well and the air above it in block-based drop freezing
178 setups (Beall et al., 2017). We anticipate vertical gradients to be reduced in DRINCZ due to the direct contact between the
179 cooling medium (ethanol) and the well tray. Therefore, we incorporated a bath leveler composed of a level sensor and solenoid
180 valve to ensure that the ethanol level remains constant. The level sensor (Honeywell LLE 102101 liquid level sensor) detects
181 when the ethanol falls below a fixed level relative to the wells and triggers the solenoid valve (Kuhnke 64.025, 12 VDC valve)
182 to open, allowing additional ethanol to flow into the bath. The level sensor and solenoid are monitored and controlled using a
183 ‘sketch’ written in Arduino (Arduino Uno Rev3 SMD). In order to minimize thermal gradients by adding warm ethanol to the
184 bath, the ethanol is precooled to 0 °C using an ice water bath and then added through a copper pipe that extends to the bottom
185 of the bath. Thus, the bath leveler ensures that the wells remain in good thermal contact due to a constant level of ethanol
186 during experiments, while minimizing temperature fluctuations within the bath. The resulting increased reproducibility of
187 experiments due to the bath leveler is discussed in section 3.4.

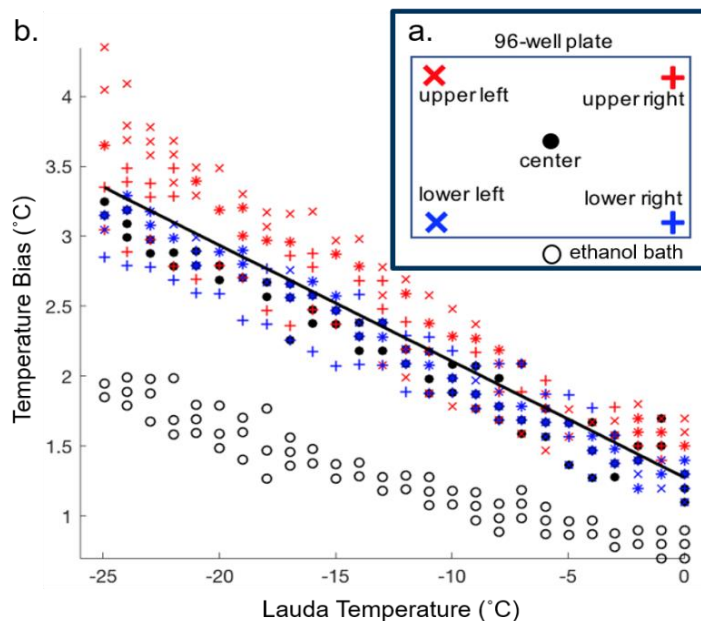
188 **3 Validation**

189 The validation of the instrument is presented in four sections, with the first discussing the temperature calibration followed by
190 discussing the observed bias in freezing, the quantification of instrumental uncertainty and lastly, the improved reproducibility
191 of DRINCZ due to the addition of the bath leveller.

192 **3.1 Temperature Calibration**

193 The temperature reported as the freezing temperature is based on the ethanol bath temperature measured by the Lauda chiller
194 (T_{lauda}). In order to correct for the difference between the temperatures of the sample in the wells (T_{well}) and T_{lauda} , a temperature
195 calibration was performed. The calibration was conducted by measuring the temperature (Type K thermocouple) within the
196 four corner wells and a center well of the 96-well tray (Fig. 3a). The same thermocouple was used for all the well temperature
197 measurements to avoid biases between different thermocouples. The wells were filled with 50 μL of ethanol instead of water
198 to extend the calibration across the entire experimental temperature range of DRINCZ without the interference of freezing.
199 The temperature bias between the wells and T_{lauda} was measured every 1 °C while the bath was cooled at the typical ramp rate
200 of 1 °C min^{-1} . The calibration was performed three times for each well (Fig 3b). Not surprisingly, we found that the ethanol
201 temperature in the bath was consistently lower than the temperature in the five calibration wells and the difference between

202 bath and well temperature increased linearly as the bath temperature decreased. Based on these results the linear function
 203 $T_{corr} = 0.917 * T_{lauda} + 1.3$, with T_{lauda} in °C (black line in Fig. 3b) was derived to correct the well temperature. The
 204 maximum standard deviation taken as the temperature difference between the temperature fit and the individual well
 205 temperature was ± 0.6 °C.



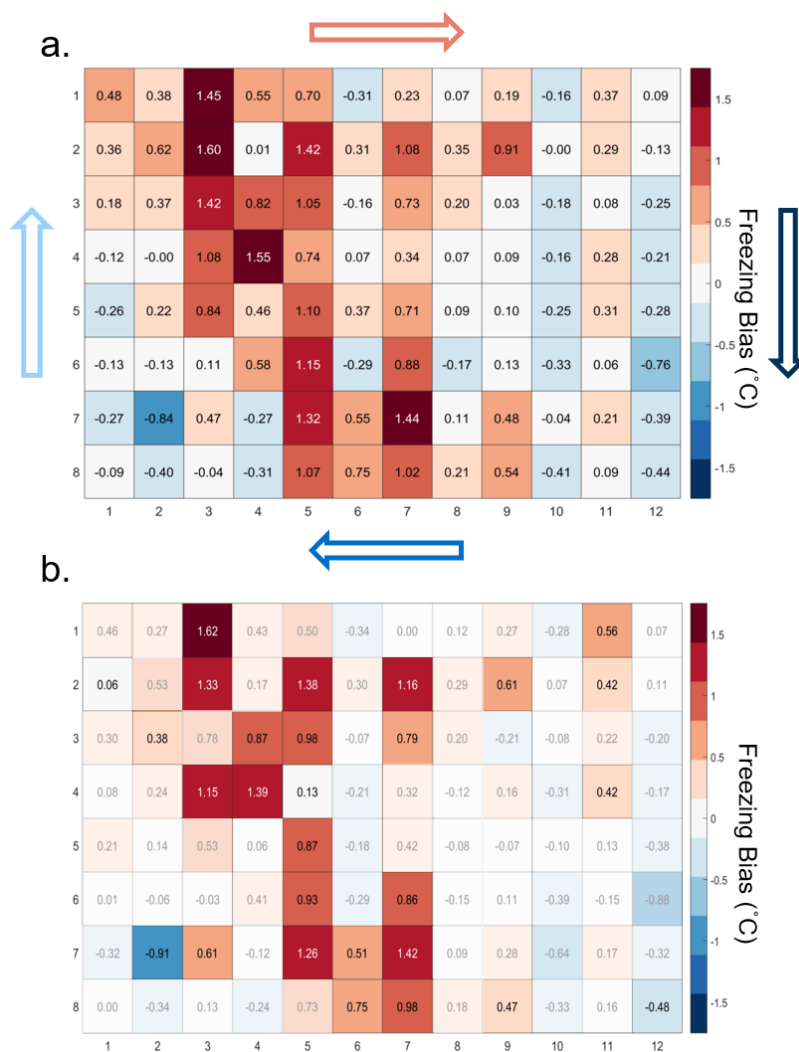
206

207 **Figure 3: (a) Locations of the type-K thermocouples tested during the temperature calibration. Additionally, the temperature**
 208 **difference between the Lauda temperature and the ethanol bath was measured at the indicated location (black open circle).** (b) **The**
 209 **temperature bias between the wells and ethanol bath is displayed versus the Lauda bath temperature. The linear temperature**
 210 **correction is shown in black.**

211 3.2 Freezing Bias across the 96-well Tray

212 The temperature calibration discussed above revealed potential variations in the well temperatures between the corner and the
 213 center wells. We thus quantified the bias for individual wells, but conclude that it is within the instrument experimental error
 214 as discussed below. To do so, 20 pure water (Molecular Biology Reagent, W4502 SigmaAldrich; hereafter referred to as SA
 215 water) experiments were analyzed. SA water was chosen for this analysis due to its homogeneity and low freezing temperature,
 216 where the observed spread in well temperature was maximized (see Fig. 3). For each well the median freezing temperature (or
 217 temperature when frozen fraction (FF) = 0.5) (\tilde{w}_i) was compared to the median freezing temperature of the 4 corner wells
 218 (\tilde{w}_{4ref}) used for the temperature calibration (see Fig. 3a and Fig. A2 for the distribution in freezing temperatures of the wells).
 219 The difference between \tilde{w}_{4ref} and \tilde{w}_i ($\tilde{w}_{4ref} - \tilde{w}_i$) is shown in Fig. 4a. The red (blue) shading indicates a warm (cold)
 220 bias and signifies that the solution in these wells are exposed to warmer (colder) temperatures than the average of the four
 221 reference wells. The higher concentration of red shades in the middle of the tray suggests that the center of the tray is exposed to as much

222 as 1.5 °C warmer ethanol flow than the tray periphery. Indeed, the chilled ethanol circulates clockwise in the Lauda chiller and
 223 thus the freezing appears to track the flow (arrows in Fig. 4). Thus, the ethanol circulation explains the observed bias in freezing
 224 temperatures across the well plate. The same analysis procedure was applied to the same 20 samples separated by user (12 and
 225 8 experiments) and a similar bias was observed (see Appendix Fig. A3). Therefore, the reported bias is instrumental,
 226 reproducible and any potential user bias can be excluded. The bias was found to be statistically significant at the 95%
 227 confidence interval for 30% of the wells and resulted in an overall bias of 0.23 °C (see Fig 4b and Appendix A). As such, a
 228 well by well bias correction was developed and tested as described in Appendix A. Although the bias correction performed as
 229 expected, the bias of 0.23 °C falls within the instrumental uncertainty as discussed in Section 3.3 and is therefore not applied
 230 to DRINCZ measurements by default. Nevertheless, the potential benefits and impacts of a bias correction is discussed in the
 231 following section.



232

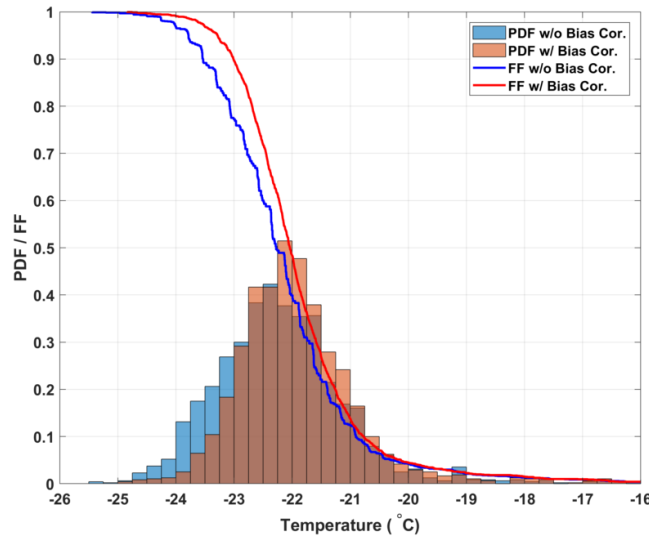
233 **Figure 4:** (a) Bias in the freezing of SA water ($\bar{w}_{4ref} - \bar{w}_i$ in °C) based on the median value of each well over 20 experiments relative
 234 to the median temperature of freezing for the 4 corner wells used during the temperature calibration. A positive (negative) bias
 235 indicates that the wells experience a warmer (colder) temperature than the four corner wells used for temperature calibration and
 236 therefore freeze at lower (higher) temperatures than reported. The arrows represent the ethanol circulation in the chiller and the
 237 color represents the temperature trend of the ethanol as it circulates in the bath with dark blue being the coldest and red the warmest.
 238 (b) Mean freezing bias of SA water between the four reference wells and each well ($\bar{w}_{4ref} - \bar{w}_i$). Positive (negative) values indicate,
 239 as denoted by shades of red (blue), wells that systematically freeze at colder (warmer) temperatures and therefore experience warmer
 240 (colder) temperatures than reported. Statistically insignificant biases as determined by a Welch's *t*-test (see Eq. A1) are depicted as
 241 greyed out.

242 3.2.1 Impact of Bias Correction on Frozen Fraction

243 By accounting for the bias in freezing temperature across the 96-well tray by first applying the temperature calibration and
 244 then the bias correction such that corrected well value ($\bar{\bar{w}}_i$) becomes:

$$245 \bar{\bar{w}}_i = \bar{w}_i + (\bar{w}_{4ref} - \bar{w}_i), \quad (6)$$

246 the slope of the *FF* curves steepens and becomes smoother, which is expected as the observed freezing temperatures become
 247 more constrained (see Fig. 5). Although the median freezing temperature with and without the bias correction only changes by
 248 0.2 °C (consistent with the correction of the mean bias of 0.23 °C found above), the narrowing of the freezing temperature
 249 distribution is significant at the 95% significance level (Welch's *t*-test, see Eq. A1). This result shows that by using the spatial
 250 dependent freezing information of a well from optically based drop freezing instruments like DRINCZ, temperature can be
 251 better constrained. Such a bias correction should also be applicable to freezing methods that use block based cooling, where
 252 gradients across the block have been observed or modelled (Beall et al., 2017; Harrison et al., 2018).



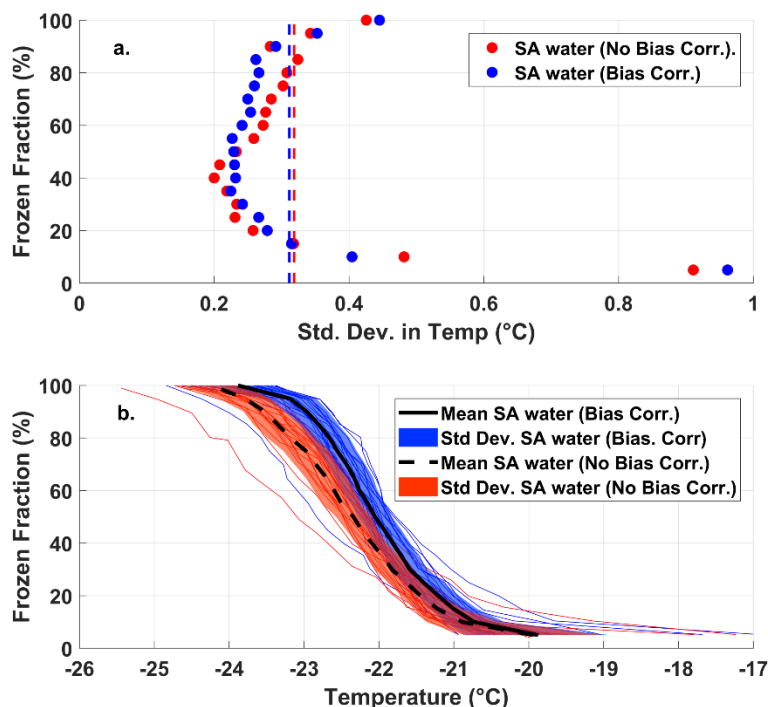
253 **Figure 5:** Histograms representing the probability distribution functions for freezing temperatures of the 20 SA water experiments
 254 without (blue bars) and with the bias correction (red bars). The calculated cumulative distribution functions, or frozen fraction
 255 curves without and with the bias correction are represented as the blue and red lines, respectively.
 256

258 **3.3 Instrument Uncertainty**

259 The instrumental uncertainty for DRINCZ is assessed by using the standard deviation in the observed freezing temperatures
260 of the SA water experiments across all wells in combination with the error in the temperature of the wells established during
261 the temperature calibration. The standard deviation of the freezing temperature of the SA water is dependent on FF , with a
262 minimum at $0.5 FF$ (Fig. 6a). This dependence is expected as the $0.5 FF$ corresponds to the most likely temperature for the
263 SA water to freeze and therefore, should show the least variability across the 20 experiments used in the analysis. Furthermore,
264 by using the $0.5 FF$ the influence of contamination and outliers is minimized. The standard deviation at each FF is the
265 uncertainty due to the instrument as well as the variability in the freezing temperature of the SA water and represents the upper
266 limit of the instrumental uncertainty. Given the contribution to the uncertainty due to the variability of the freezing temperature
267 of the SA water, the standard deviation at $FF = 0.5$ can be used as the upper limit of the instrumental uncertainty across the
268 entire FF range. Incorporating a bias correction results in a negligible average difference in the standard deviation (as shown
269 by dashed lines in Fig. 6a). Thus, the upper limit of the instrumental precision is ± 0.3 °C (the mean of the standard deviation
270 of freezing temperature over the entire freezing spectrum).

271

272 Although the instrumental precision indicates that DRINCZ is very reproducible (± 0.3 °C), the accuracy in the reported
273 temperature must be accounted for. Based on the temperature calibration, the standard deviation of the well temperatures is
274 temperature dependent. At the coldest temperatures of the freezing range of the SA water (~ -25 °C), the standard deviation of
275 the well temperatures is largest, likely due to the increased gradient between the bath and air temperature and therefore, the
276 importance of the ethanol circulation through the bath is increased. To account for this temperature dependence, the maximum
277 standard deviation of ± 0.6 °C from the temperature calibration, corresponding to the lowest observable freezing temperature
278 in DRINCZ (freezing temperature of SA water) is used. Therefore, when accounting for both the precision of the measurements
279 and the accuracy of the temperature, the overall uncertainty of the reported freezing temperature of a well in DRINCZ is
280 ± 0.9 °C. This value is comparable to other recently developed drop freezing techniques, which report uncertainties ranging
281 between ± 0.9 °C (Harrison et al., 2018) and ± 2.2 °C (Beall et al., 2017).



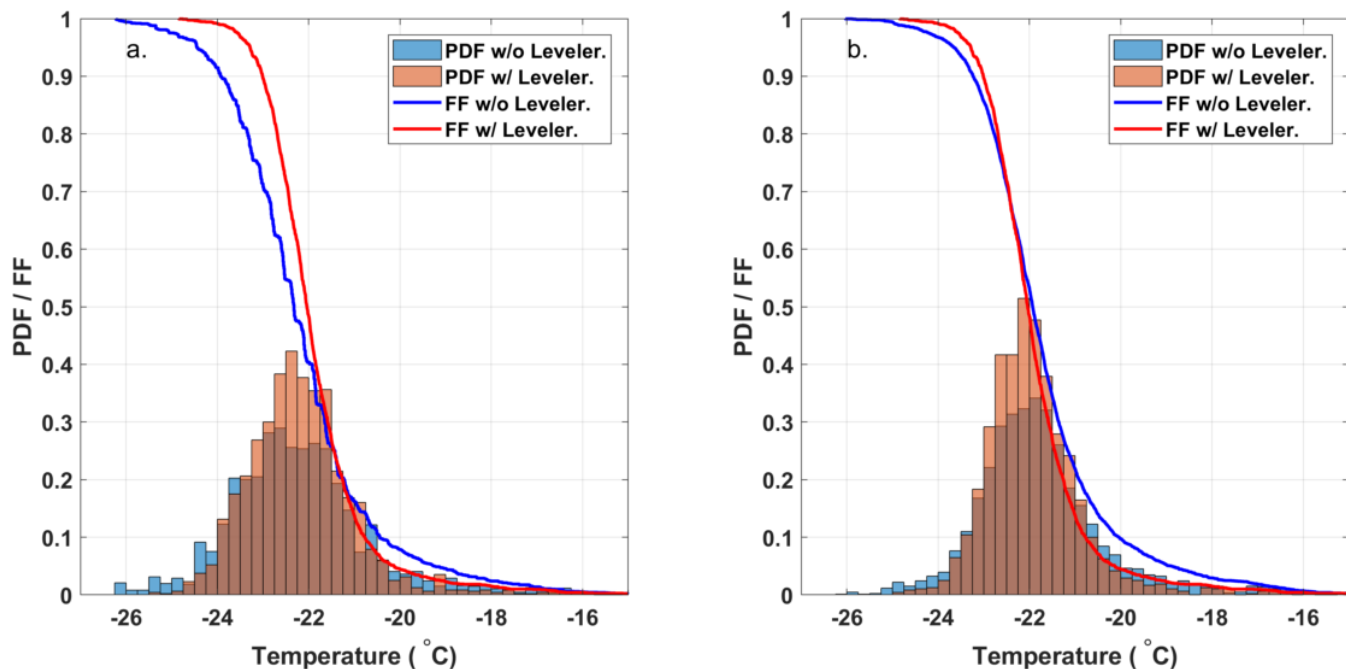
282

283 **Figure 6:** (a) *FF* and the corresponding standard deviation of the freezing temperatures from the 20 SA experiments with and
 284 without the bias correction shown as blue and red dots, respectively. The red and blue dashed lines represent the standard deviations
 285 in temperature averaged over all *FF* values without and with the bias correction, respectively. (b) The *FF* of the 20 SA water
 286 experiments as a function of temperature with and without the bias correction (thin blue and red lines, respectively). The color fill
 287 represents the standard deviations of the SA water from the mean freezing temperature with (solid black line) and without (the
 288 dashed black line) the bias correction.

289

290 3.4 Importance of the Bath Leveler

291 To assess the impact of the decreasing ethanol level on experiments in DRINCZ, 32 experiments with SA water without a bath
 292 leveler were compared to the 20 SA water with a bath level sensor, the same 20 SA water discussed in the previous section.
 293 Figure 7a shows that the bath sensor reduces the spread in freezing temperatures observed. The decrease in the 0.5 *FF*
 294 temperature without the bath leveler is due to a larger gradient between the aliquot and the bath temperatures, thus the well is
 295 warmer than expected, requiring further cooling to observe freezing. The additional cooling in combination with the variable
 296 starting level of the ethanol relative to the wells in the cases of no bath leveler is responsible for the longer freezing tail of the
 297 *FF* curve (blue line) at higher *FF*s. Without the bath leveler, the initial height of ethanol relative to the wells is user dependent
 298 and not reproducible, leading to both the higher and lower observed freezing temperatures.



299

300

301

302

Figure 7: (a) Comparison of the freezing temperature of SA water without (32 experiments, blue) and with (20 experiments, red) the bath leveler. The histograms are normalized to represent the PDF of the freezing temperatures and the lines represent the mean FF curves of the SA water experiments. (b) Shows the same as panel a, except that a bias correction is applied to both sets of experiments.

303

304

305

306

307

308

309

310

311

312

Although the median freezing temperature ($FF=0.5$) only decreased by $0.25\text{ }^{\circ}\text{C}$ without the bath leveler, the freezing curves steepen when the bath leveler is incorporated in DRINCZ, leading to a decrease of the standard deviation from ± 1.4 to $\pm 1.0\text{ }^{\circ}\text{C}$ over the entire FF range. A bias correction applied following the procedure in Section 3.2 reduces the issues associated with a variable bath leveler as seen by the similar FF curves and histograms normalized using the probability density function (PDF) estimate in Fig. 7b for experiments with and without the bath leveler. The difference in mean freezing temperatures decrease to $0.05\text{ }^{\circ}\text{C}$ at $FF=0.5$ and the standard deviation of the SA water freezing temperature without the leveler decreases from ± 1.4 to $\pm 1.2\text{ }^{\circ}\text{C}$ over the entire FF range. This decrease is expected as the bias correction is designed to reduce the spread in freezing temperatures within the 96 aliquots. Although the bias correction reduces the need for a bath leveler in DRINCZ, the bias is instrument dependent and may be less pronounced in other drop freezing setups. Therefore, we recommend the use of a bath leveler in any bath-based drop freezing device.

313

4 Freezing Experiments

314

315

316

317

To verify the performance of DRINCZ in the context of other published drop freezing techniques, we use the SA water experiments to characterize the instrumental background (Section 4.1) and perform freezing experiments with NX-illite suspensions (Section 4.2). To demonstrate applicability of the instrument to analysis of field samples, the evolution of the ice nucleating ability of atmospheric aerosol particles collected in snow samples at the Sonnblick Observatory in the Hohe Tauern

318 region of Austria during a mid-latitude storm system is assessed in Section 4.3. Lastly, some uncertainties associated with
 319 measuring INP in snow samples (Section 4.4) and further validation of DRINCZ through dilutions are discussed (Section 4.5).
 320

321 4.1 Background of DRINCZ

322 The background freezing due to the experimental technique and the SA water used to suspend and dilute samples must be
 323 known to discriminate freezing events due to the sample from freezing events due to the water used. Furthermore, an SA water
 324 sample is run as a standard at the beginning of each measurement day to ensure the system is operating correctly. The 20 SA
 325 water experiments are therefore used to assess the instrument background freezing. It is important to note that in cases where
 326 solvents other than SA water are used or where contamination from a sampling technique (e.g. snow collection or impinger
 327 measurements) is possible, a different background calculation must be used to accurately assess the freezing ability of a sample.
 328 The background of DRINCZ when used with SA water, is calculated by fitting the 20 SA water experiments with a five
 329 parameter Boltzmann fit. The five parameter version was chosen to account for asymmetry (Spiess et al., 2008) in the freezing
 330 of the SA water but due to the minimum and maximum values of FF given as 0 and 1, respectively, the fit reduces to three
 331 parameters and takes the form:

$$332 FF_{BGfit}(T_{frzBG}, a, b, c) = \frac{1}{\left(1 + e^{a(T_{frzBG} - b)}\right)^c}, \quad (8)$$

333 where FF_{BGfit} is the fitted FF of the SA water as a function of the observed freezing temperatures of the SA water, T_{frzBG} ,
 334 and the fitting parameters, a , b , c represent the slope of the fit ($a = 1.9651$), the inflection point ($b = -22.7134$) and the
 335 asymmetry factor ($c = 0.6160$), respectively. The value of 1 in the numerator represents the maximum FF . The fit and
 336 associated coefficients (including 95% confidence range and r^2) are shown in Table 1 and Fig. 8 respectively.

337

338 **Table 1: Coefficients for the three parameter Boltzmann fit of the SA water freezing background and 95th percentile confidence**
 339 **interval bound values.**

	a	b	c	r^2
Best	1.9651	-22.7134	0.6160	0.97
-95 th %	1.7254	-22.8955	0.4683	N/A
+95 th %	2.2049	-22.5312	0.7637	N/A

340

341 The fitted freezing background is used to correct for the contribution of SA water to the observed freezing of a sample. To
 342 account for the presence of multiple ice nucleating particles coexisting in a single well, the background is removed by
 343 subtracting the differential nucleus concentration of the background from that of the sample (Vali, 1971, 2019). The differential
 344 nucleus concentration ($k(T)$) is initially defined in Vali (1971) as:

345
$$k(T) = -\frac{1}{V_a \Delta T} \cdot \ln\left(1 - \frac{\Delta N}{N(T)}\right), \quad (9)$$

346 where $N(T)$ is the number of unfrozen aliquots at the beginning of a temperature step while ΔN is the number of aliquots that
 347 freeze during the temperature step (between pictures) or ΔT .

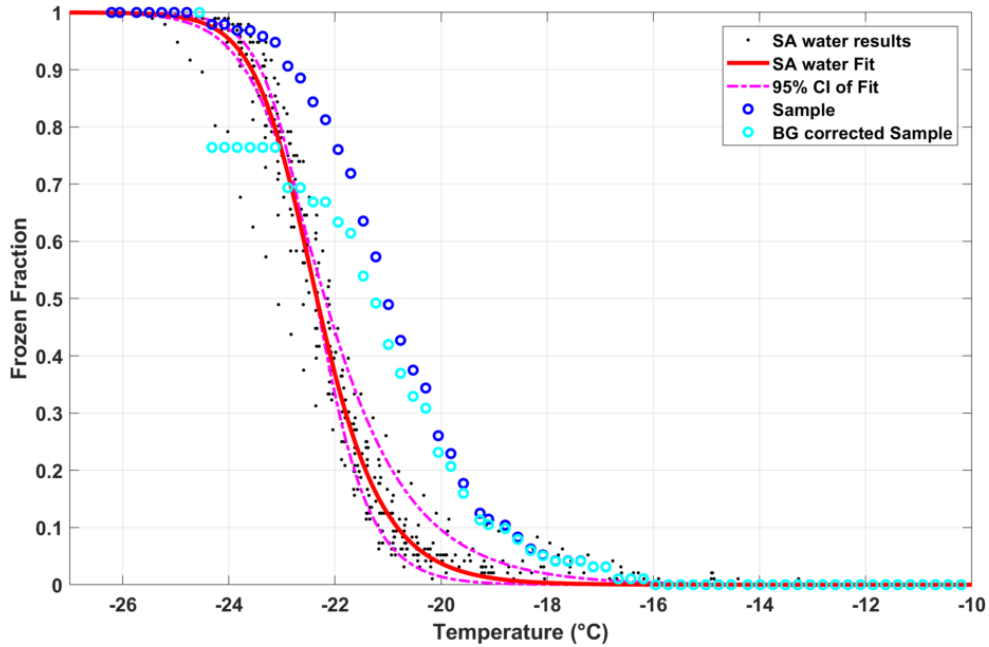
348 The background corrected differential nucleus concentration ($k_{corr}(T)$) is obtained by:

349
$$k_{corr}(T) = k_{sam}(T) - k_{bg}(T), \quad (10)$$

350 where $k_{sam}(T)$ and $k_{bg}(T)$ are the sample and background differential nucleus concentration, respectively. The background
 351 corrected $FF_{cor}(T)$ is then achieved by inverting Eq. 9 and taking the cumulative sum of $k_{corr}(T)$:

352
$$FF_{cor}(T) = 1 - \exp(-\sum[k_{corr}(T) \cdot \Delta T] \cdot V_a), \quad (11)$$

353 An example of the impact of the background correction on the FF of the diluted snow sample collected on Nov 30th 2017
 354 (discussed in section 4.3) is shown in Fig. 8.



355
 356 **Figure 8:** SA water data (black dots) and corresponding fit (red line, Eq. 8) including the 95th percentile confidence interval (dashed-
 357 dot magenta lines). The blue circles represents the diluted snow sample collected on Nov 30th 2017 which is then corrected for the
 358 contributions of freezing from the SA water using the background correction ($FF_{cor}(T)$ as described in Eq. 11; cyan circles).

359
 360 **4.2 Comparison of DRINCZ to other immersion freezing techniques**

361 To validate the performance of DRINCZ, we use different wt. % NX-illite suspensions to compare the results from DRINCZ
 362 to those summarized in Hiranuma et al. (2015), Beall et al. (2017) and Harrison et al. (2018). In the atmosphere, illite constitutes
 363 up to ~40 % of the transported dust fraction (Broadley et al., 2012; Murray et al., 2012), making it an excellent surrogate for
 364 atmospherically relevant dust. An initial stock suspension of 0.1 wt. % NX-illite was prepared with SA water and then diluted

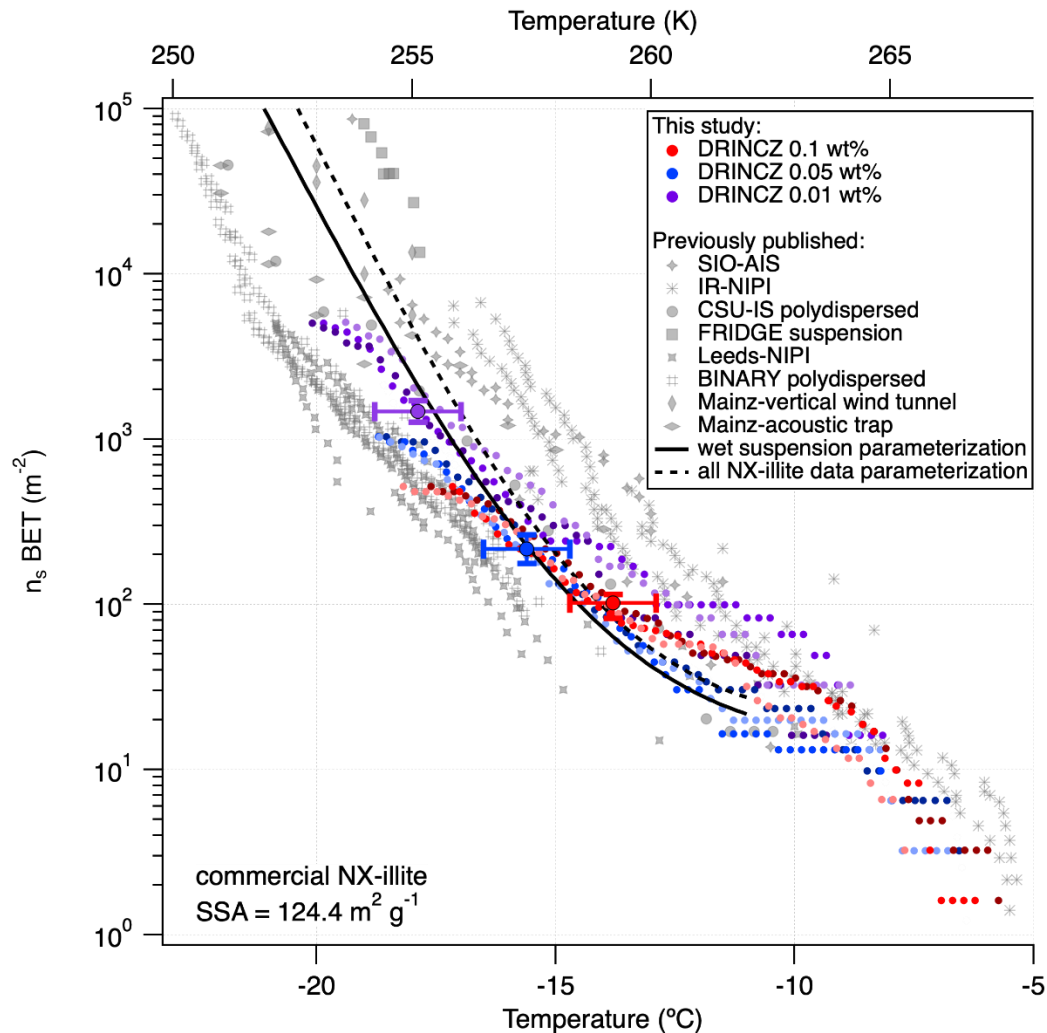
365 to produce mass concentrations of NX-illite of 0.05 and 0.01 wt. %. The suspensions were manually shaken for 30 s, poured
366 into a dispensing tray and then immediately pipetted into the well plate. Triplicates of each suspension concentration were
367 investigated with DRINCZ (see Fig. A4 for FF curves) and then normalized to the number of active sites per BET-derived
368 surface area (n_{sBET}) using a variation of Eq. 2 as follows:

$$369 \quad n_{sBET} = - \frac{\ln(1-FF)}{V_a * SA_{BET} * C_{NX}}, \quad (12)$$

370 where SA_{BET} is the BET surface area of the particles used (NX-illite) and C_{NX} is the mass concentration of NX-illite in an
371 experiment.

372

373 The n_{sBET} of NX-illite calculated using Eq. 12 from the measurements made with DRINCZ and background corrected (using
374 Eq. 11) falls within the results from Hiranuma et al. (2015), Beall et al. (2017) and Harrison et al. (2018) (Fig. 9). In theory,
375 n_{sBET} should be insensitive to concentration as the number of ice nucleating sites is normalized to the total surface area. Indeed,
376 the differing weight percent samples overlap to an extent (Fig. 9). Furthermore, the lower-weight-percentage samples extend
377 the observable n_{sBET} to higher values and colder temperatures. Similar to the observations of Harrison et al. (2018), the data
378 points from the 0.01 wt. % suspension appear as outliers at the warmest temperatures. However, it is not possible to determine
379 if these outliers are due to random freezing events that occur at high temperatures and therefore produce elevated cumulative
380 n_{sBET} values at lower temperatures or if they are due to an uneven distribution of the active sites in each aliquot that may
381 result from diluting a single stock suspension rather than preparing individual weight percent suspensions (Harrison et al.,
382 2018). Thus a spread equivalent to or less than the spread in the concentrations, up to an order of magnitude in this case, can
383 be expected. Furthermore, considering the ± 0.9 °C uncertainty, depicted by the horizontal error bars, the differences between
384 concentrations are not significant. They fall within the same range as the measurements of Beall et al. (2017) and between
385 BINARY and Leeds-NIPI and IR-NIPI at colder temperatures (Fig. 9). The overlap between the n_{sBET} measured with DRINCZ
386 and the NX-illite parameterization (Hiranuma et al., 2015) indicate that DRINCZ is capable of accurately measuring the
387 concentration of INPs and their active sites in the immersion freezing mode (Fig. 9).



388

389 **Figure 9:** Triplicates of n_{sBET} (depicted by shading of the same color) as a function of temperature for three concentrations of NX-
 390 illite, $10^{-3} \text{ g ml}^{-1}$ (red dots), $5 \times 10^{-4} \text{ g ml}^{-1}$ (blue dots) and $10^{-4} \text{ g ml}^{-1}$ (purple dots), measured by DRINCZ. An example of the
 391 temperature uncertainty and the uncertainty due to the background correction are depicted for each weight percent as horizontal
 392 and vertical error bars, respectively. Literature values from Hiranuma et al, (2015), Beall et al, (2017) and Harrison et al, (2018)
 393 are shown for comparison. n_{sBET} was calculated using a BET surface area of $124.4 \text{ m}^2 \text{ g}^{-1}$ (Hiranuma et al., 2015).

394

395 4.3 Ice Nucleating Particle Concentrations in Snow Samples from a Mountaintop Observatory in Austria

396 In order to demonstrate the performance of DRINCZ, snow samples collected between the 27th and 30th of November 2017 at
 397 the Sonnblick Observatory (SBO) were analyzed. The SBO is located at 3106 m on the summit of Mt. Sonnblick in the Hohe
 398 Tauern Region of Austria and has previously been used for cloud microphysical measurements (e.g. Beck et al., 2018;
 399 Puxbaum and Tschewenka, 1998). Freshly fallen snow was collected from a wind-sheltered area where the snow could not
 400 drift. A stainless steel shovel (Roth) was conditioned with snow by turning (10 times) in the surface snow next to the sampling

401 site prior to sampling. The snow was then sampled into sterile NascoWhirlPaks (Roth) and then melted at room temperature
402 (20 °C), immediately after which aliquots of snow-meltwater were filled into sterile centrifugation tubes (15 ml, Falcon tubes)
403 and stored at -20 °C. The samples were shipped and stored frozen until processed with DRINCZ at the Atmospheric Physics
404 Laboratory at ETH Zurich, to minimize any bacterial growth or changes due to liquid storage (Stopelli et al., 2014). The
405 snowfall collected at SBO occurred during two snowfall events. The first event began on the 25th and ended overnight on the
406 26th (early hours of the 27th) while the second event (28th -30th) was associated with an intensifying upper level trough, a
407 developing surface cyclone, a strong cold front and an associated secondary low (see Fig. A5 and A6).

408
409 The frozen fractions of five different snow samples were determined using DRINCZ and the cumulative concentration of
410 active sites (or $INP(T)$, see Eq. 1) were normalized to per L of meltwater (n_{mw}) (Fig. 10). Overall, the n_{mw} of the snow samples
411 fall within the range of previously reported values for precipitation samples (Petters and Wright, 2015) except for the
412 November 30th sample. Within these samples, we identify (1) a particularly active snow sample (Nov 28th), (2) samples having
413 intermediate IN activity (Nov 27, 29), and (3) a least active sample (Nov 30th). We attempt to compare these snow samples
414 based on their air mass origin.

415
416 The snowfall sampled on the 28th had the highest n_{mw} of all collected samples (Fig. 10). The meteorological conditions and a
417 comparison of back trajectories indicate that the air mass was associated with the warm sector of a synoptic system (Fig. A7)
418 that originated from North America and the North Atlantic that then crossed France and Switzerland, before arriving at SBO
419 (Fig. A8). In contrast, the arctic air mass responsible for the snowfall sampled on the 27th originated over Svalbard before
420 crossing Iceland, the British Isles, Northern France and Germany (Fig. A8).

421
422 Even though the local conditions at SBO did not change significantly between the 28th and 29th, a decrease in n_{mw} was observed
423 relative to the 28th and n_{mw} gradually decreased between the first and second sample on the 29th (Fig. 10). The back trajectories
424 show that the origin of the air mass changed from North America and the North Atlantic on the 28th to exclusively originating
425 over the North Atlantic on the 29th (Fig. A8). Additionally some of the back trajectories on the 29th show an increased
426 interaction with the boundary layer over Europe (Fig. A8). Nevertheless, the decrease in n_{mw} suggests that if boundary layer
427 aerosols from parts of Europe did reach the precipitating clouds at the SBO, they are less efficient INPs than the marine aerosols
428 (Lacher et al., 2017, 2018) associated with the samples on the 27th and 28th.

429
430 Finally, the lowest n_{mw} observed were from meltwater collected on the 30th. The cold frontal passage and associated cold air
431 advection caused the temperature to drop by 6 °C by noon on the 30th (Fig. A7) and the n_{mw} in the associated snowfall decreased
432 substantially, exceeding the lower limit of previously reported n_{mw} values (Petters and Wright, 2015, Fig. 10). The decrease in
433 n_{mw} , however, cannot be explained solely on the origin of the air mass as the arctic air mass on the 27th also crossed similar
434 parts of the UK or had significant interaction with the marine boundary layer. Nevertheless, the concentration of INPs in the

435 sea surface microlayer is variable and the efficiency of emitting marine INP from the surface is wind speed dependent (DeMott
436 et al., 2016; Irish et al., 2017; McCluskey et al., 2018; Wilson et al., 2015). Therefore, even though the trajectories on the 27th
437 and 30th interacted with the marine boundary layer, they may contain different concentrations of INPs, yielding the observed
438 differences in n_{mw} . In addition to air mass origin, it has been shown that precipitation efficiently removes INP and thus
439 influences n_{mw} (Stopelli et al., 2015). Indeed, the most upstream precipitation (see Fig. A8) corresponds to the sample collected
440 on the 30th, which has the lowest n_{mw} . Therefore, the most efficient INPs could have been removed in the upstream
441 precipitation, contributing to the observed decrease in n_{mw} .

442
443 The differences in n_{mw} could not be rectified by a single metric in this study but rather a combination of factors likely led to
444 the observed variability. In particular, as the warm sector of the cyclone approached the sampling site (28th), n_{mw} increased.
445 Conversely, after cold frontal passage (30th) the n_{mw} decreased. Back trajectories indicate that the air mass source region and
446 the amount of upstream precipitation differed between the two sectors of the cyclone. This result is consistent with previous
447 studies that suggest that air mass origin (e.g. Ault et al., 2011; Creamean et al., 2013; Field et al., 2006; Lacher et al., 2017,
448 2018) and upstream precipitation (Stopelli et al., 2015) influences the INP concentration. Furthermore, the dependence on the
449 long range air mass history to the observed variability in n_{mw} suggests that local sources are not responsible for the observed
450 INPs.

451 **4.4 Limitations of snow meltwater sample comparisons**

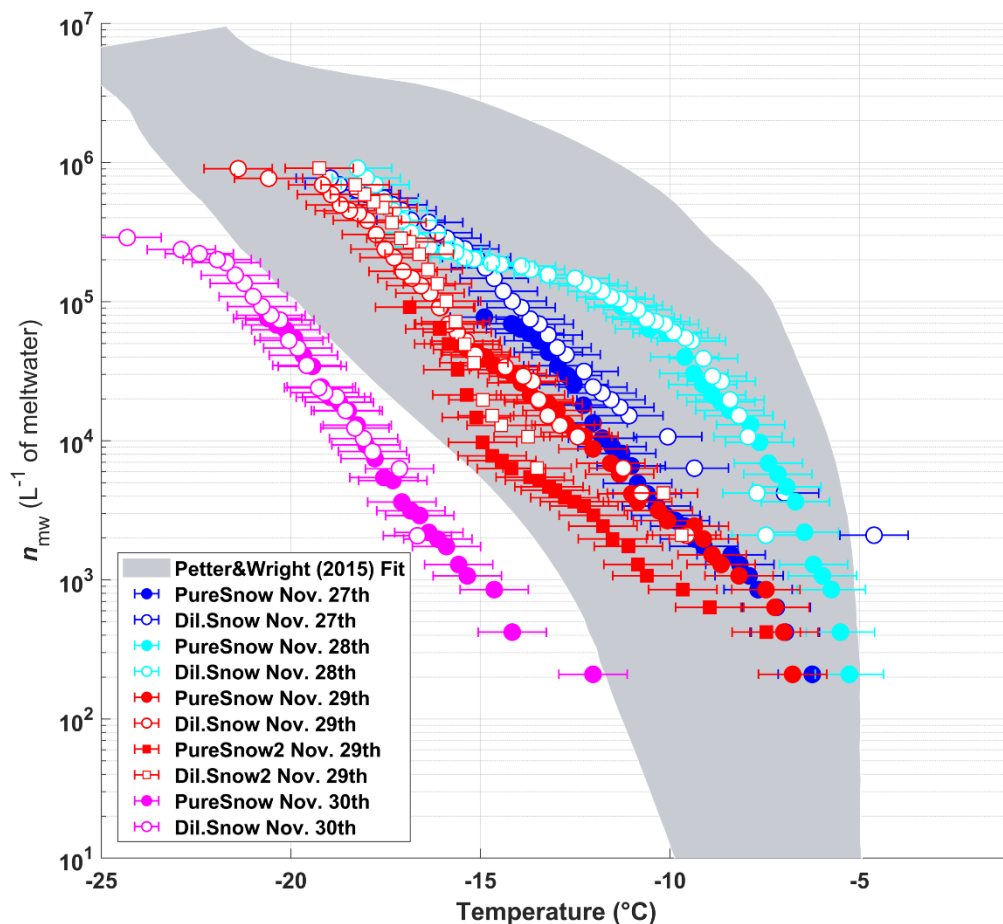
452 One limitation when comparing snow samples collected at different times and locations is the unknown number of aerosols,
453 INPs and ice crystals that contributed to the collected meltwater. Since n_{mw} depends on the number and mass of the ice crystals
454 within a snow sample, the melt water volume or density of each snowflake influences n_{mw} . For example, snow to liquid ratios,
455 which can be used as a proxy for snow flake density and melt water equivalent, can vary between 5 to 1 in heavy wet snow
456 and 100 to 1 in powdery snow (Roebber et al., 2003). However, even when considering this variability in the required amount
457 of snow to produce the same volume of ice crystal melt water, n_{mw} would only differ by a factor of 20. As can be seen in
458 Fig. 10, n_{mw} varies by two orders of magnitude or more between the 28th and the 30th of November and the difference is
459 therefore robust. Additionally, heavy wet snow has been found to occur in the warm core of a synoptic system while lighter,
460 more powdery snow was found in the air mass after cold frontal passage, where air temperatures are colder (Roebber et al.,
461 2003). As the n_{mw} on the 28th was collected in the warm sector and the sample on the 30th was post cold front, differences in
462 snow density may lead to an underestimation in the difference between the n_{mw} of these two samples. Therefore, we recommend
463 that future studies also consider the snow water equivalent when comparing the n_{mw} as this could influence n_{mw} by a factor of
464 20 or more.

465
466 Another uncertainty with using precipitation samples for analyzing INP concentrations is associated with aerosol scavenging
467 and chemical ageing (e.g. Petters and Wright, 2015). As previously mentioned, the samples were stored frozen to avoid any

468 decrease in ice nucleating ability associated with storage (Stopelli et al., 2014) and therefore degradation is likely not an issue
469 in this study (Wex et al., 2019). The ability of a falling ice crystal to scavenge aerosols or rime cloud droplets depends on the
470 ice crystal habit, size, and the difference between the fall velocity of the crystal and the interstitial aerosol or cloud droplets.
471 With the exception of interstitial aerosol concentration which has been shown to influence n_{mw} by a factor of 2 (Petters and
472 Wright, 2015), these factors are all important when estimating snow density and thus make it difficult to disentangle their
473 effects on n_{mw} . Therefore, there is value in future studies of INP in MPCs to investigate the INP concentrations in cloud water,
474 interstitial aerosols and snow samples.

475 **4.5 Ice Nucleating Particle Concentrations in Diluted Snow Samples**

476 In order to extend the reported temperature range of DRINCZ, the snow samples were also diluted by a factor of 10 with SA
477 water (see Eq. 2). The dilutions (open symbols) overlay the pure samples except at the warmest temperatures where, as
478 previously mentioned, a single freezing event can lead to an increase in n_{mw} of an order of magnitude relative to the undiluted
479 sample. This effect is especially evident on the 27th when the first few wells of the diluted sample (open blue circles) froze at
480 the same or higher temperatures than the undiluted sample (filled blue circles) and led to an increase in n_{mw} of up to an order
481 of magnitude. However, this issue has been previously observed when diluting from stock suspensions (Harrison et al., 2018)
482 which is similar to diluting a snow water sample. Therefore, the dilutions further validate DRINCZ as an INP measurement
483 technique.



484

485 **Figure 10:** The cumulative number of active sites per L of meltwater (n_{mw}) of snow for undiluted snow (filled) and of snow samples
 486 diluted by a factor of 10 (white-filled symbols) as a function of temperature. The colors represent the different sampling days. On
 487 the 29th of Nov. two samples were taken and the second sample of the day is indicated by square symbols. The shaded area represents
 488 the previously reported n_{mw} from precipitation events as described in Petters and Wright (2015). The error bars represent the
 489 instrumental temperature uncertainty of ± 0.9 °C.

490 **5 Conclusions**

491 We describe and characterize DRINCZ as a newly developed drop freezing instrument for quantifying the ability of aerosols
 492 to act as ice nucleating particles in the immersion freezing mode. The instrument uncertainty is ± 0.9 °C, similar to previously
 493 published drop freezing techniques. We show that thermal contraction of ethanol as a coolant used in bath-based drop freezing
 494 techniques increases temperature variations within the sample. This issue can be corrected by incorporating a bath leveler
 495 which ensures the coolant level in the bath remains constant during an experiment. Typical drop freezing methods report
 496 temperature measured in the corner wells of a 96-well tray, at the edge of a cooling block or within the block itself (Beall et
 497 al., 2017; Hill et al., 2014; Stopelli et al., 2014). Here we show that by making use of the freezing sequence of pure water
 498 aliquots, the spatial pattern of temperature bias in the 96-well tray can be assessed. Although variations are within the

499 instrumental uncertainty of DRINCZ and are not used for DRINCZ data analysis, we present our detailed analysis of this
500 potential bias and draw attention to this issue for other drop freezing techniques. The calculated bias correction increases the
501 precision of drop freezing setups, and is an alternative to computationally expensive heat transfer simulations (Beall et al.,
502 2017). Validation experiments conducted with NX-illite showed good agreement with data reported in the literature for this
503 INP standard.

504
505 We exemplify the use of DRINCZ by measuring the concentration of INP in snow samples collected at the Sonnblick
506 Observatory in Austria. The observed INP concentrations are within previously reported values as summarized in Petters and
507 Wright, (2015) for the same temperature range as investigated here (-22 to 0 °C). Differences in INP concentration can be
508 explained by differing sectors of a mid-latitude cyclone. As the warm sector of the cyclone approached the sampling site, the
509 INP concentration increased while after the cold front passed the INP concentration decreased. Back trajectories indicate that
510 the air mass source region and the amount of upstream precipitation differed between the two sectors of the cyclone. This
511 result is consistent with previous studies that suggest that air mass origin (e.g. (Ault et al., 2011; Creamean et al., 2013; Field
512 et al., 2006; Lacher et al., 2017) and upstream precipitation (Stopelli et al., 2015) influence the INP concentration. This suggests
513 that INP in precipitation samples are likely transported from specific source regions rather than originate from local sources.
514 Thus identifying the specific sources responsible for INP and their transport pathways are essential for accurately modelling
515 the ice phase in clouds and ultimately, climate.

516 **Competing Interests**

517 The authors declare that they have no conflict of interest

518 **Code Availability**

519 The code for detecting the wells and determining when a freezing event occurs is written in MATLAB and available upon
520 request from the authors.

521 **Data Availability**

522 The data presented in this publication are available at the following DOI: <https://doi.org/10.3929/ethz-b-000369839>

523

524

525 **Author Contributions**

526 DRINCZ was developed and designed by R.O.D with the assistance of M.C.C, M.R., L.S.B, K.P.B and N.B.D. The SA water
527 experiments were conducted by M.C.C, K.P.B., L.S.B, V.W, J.W, S.B, and R.O.D. The temperature calibration and NX-illite
528 experiments were conducted and analyzed by K.P.B and N.B.D. The snow samples were collected by N.E. and analyzed by
529 R.O.D. The instrumental error, uncertainties and calibration were conducted by R.O.D. with contributions from Z.A.K and
530 C.M. The automation and analysis software was developed by R.O.D. with contributions from K.P.B and M.C.C. The well
531 plate holder was designed by M.R. and R.O.D. and manufactured by M.R. The manuscript was written by R.O.D with
532 contributions from N.B.D, C.M. and Z.A.K. The project was supervised by Z.A.K.

533 **Financial support**

534 This research has been supported by the Swiss National Science Foundation (grant no. 200021_156581)

535 **Acknowledgements**

536 Z. A. K. would like to acknowledge Franz Conen and Emillano Stopelli for assistance with the initial set up of the droplet
537 freezing assay. We are grateful to Dr. James D. Atkinson for discussions and help with experiments during the preparatory
538 phase of DRINCZ development. We acknowledge technical assistance from Hannes Wylder. R.O.D. would like to thank Dr.
539 William Ball for insightful statistical discussions, Ellen Gute for performing camera tests and Michele Gregorini for assistance
540 with the automation.

541 **Appendix A**

542 **Freezing bias by user**

543 The 20 SA water experiments were performed over a three month period by two users. The SA water was unaffected by aging
544 over this period as it originated from varying bottles distributed by the manufacturer (Sigma Aldrich). The user bias was
545 calculated the same way as the bias for all 20 experiments. The bias is relative to the median freezing temperature of the 4
546 corner wells obtained by the respective user. As can be seen in Fig. A3, the pattern of freezing bias is consistent regardless of
547 the user. This similarity indicates that the reported bias is instrumental and not user specific.

548

549 **Bias significance and correction**

550 To ensure that the observed bias is statistically significant, a two-sample, two-tailed *t*-test was performed. In particular, a
551 Welch's *t*-test was used due to the different number of samples between the combination of the 4 reference wells (20

552 experiments x 4 wells = 80 values) and each well (20 experiments x 1 well = 20 values) and the different variance of freezing
 553 for each well (Derrick and White, 2016). In a Welch's t -test the location parameter of two independent data samples is assessed
 554 as follows:

$$555 \quad t = \frac{\bar{w}_{4ref} - \bar{w}_i}{\sqrt{\frac{s_{4ref}^2}{Nw_{4ref}} + \frac{s_i^2}{Nw_i}}} \quad (A1)$$

556 where \bar{w}_{4ref} and \bar{w}_i are the mean freezing temperature of the reference wells and an individual well, respectively. s_{4ref}^2 and
 557 s_i^2 are the variances of freezing in the reference and the individual wells and Nw_{4ref} and Nw_i are the number of samples for
 558 the reference wells and an individual well, respectively. The variance of the freezing temperature of SA water in each well is
 559 shown as boxplots in the Appendix (Fig. A2). The temperature of approximately 30% of the wells was found to be statistically
 560 different from the average freezing temperature of the 4 reference wells at the 95% confidence level, with a resultant mean
 561 bias of 0.23 °C (Fig. 4b). Due to a fraction of wells with a statistically significant bias, a correction factor based on the mean
 562 bias from the 20 SA water experiments is tested for all wells excluding the 4 corner wells used as the reference to avoid
 563 overfitting the data. Of note, the reported bias is derived based on the freezing range of SA water from -16 to -26 °C. However,
 564 based on the relatively constant spread in the temperature calibration data (see Fig. 3b), it is reasonable to assume that the bias
 565 has a weak temperature dependence.

566 Although the freezing bias was shown to be representative when the SA water data was split in two (8 and 12 samples), it is
 567 still necessary to validate its robustness on a larger sample size. In order to artificially increase the sample size of the
 568 experiments, the bias was recalculated randomly such that only 90% or 18 of the experiments were used. The resultant bias
 569 correction was then applied to the remaining 10% or 2 of the experiments and tested to see if the mean freezing temperature
 570 of the bias corrected tray was closer to the reference freezing temperature of the 4 corner wells. This procedure was repeated
 571 1000 times at random. The difference in the median freezing temperature ($FF= 0.5$) and 4 corner reference wells decreased
 572 from 0.23 °C to 0.04 °C, while the standard deviation of the bias corrected data increased by 0.007 °C. Thus, the bias correction
 573 performed as expected and reduced the bias in freezing temperature. Nonetheless, this improvement falls within the uncertainty
 574 of the instrument, as discussed in Section 3.3 and is therefore not applied to DRINCZ measurements by default.

575

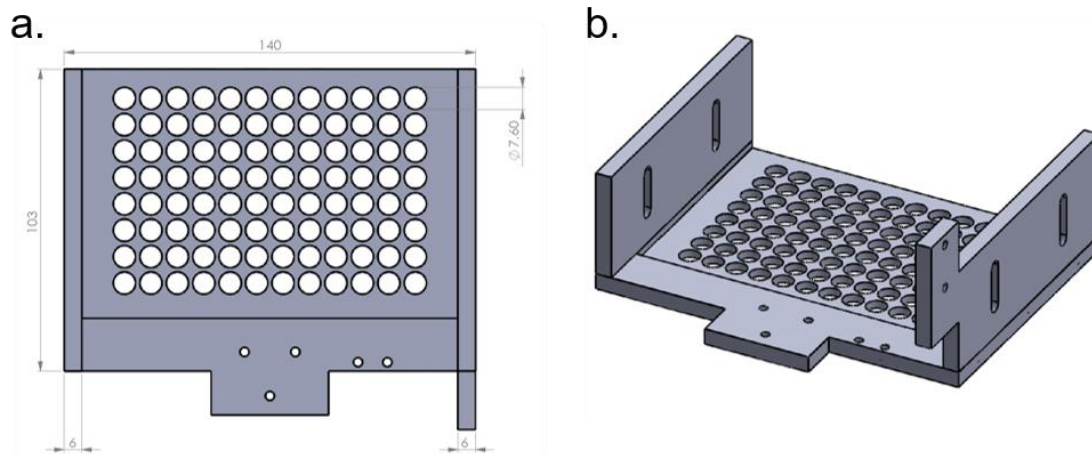
576 **Synoptic Summary Nov. 27th-30th**

577 The synoptic pattern over Europe on the 27th through 30th of November produced large variations in both temperature and air
 578 mass origin at the SBO. As can be seen from the surface pressure maps shown in Fig. A5, an evolving cyclone tracked across
 579 Northern Europe before occluding in the vicinity of Denmark. This cyclone produced strong warm advection at SBO on the
 580 27th (see Fig. A7) in advance of the approaching cold front. As the cyclone began to fill over Southern Scandinavia, the cold
 581 front stalled along the Alps and westerly flow continued at SBO from the 28th – 29th (Fig. A7). Farther west, the cold front
 582 reached the Mediterranean where a secondary low developed along the remnant baroclinic zone (Fig. A6 panel c.). This

583 secondary low traversed Italy and rapidly intensified as it crossed the Adriatic Sea before entering the northern Balkans (Fig.
584 A6 panel d.). The secondary low and an amplifying ridge over the British Isles forced the cold front over SBO at 00Z on the
585 30th when cold air advection ensued over the SBO region (Fig. A7), as shown by the back trajectories (Fig. A8.e and f.).

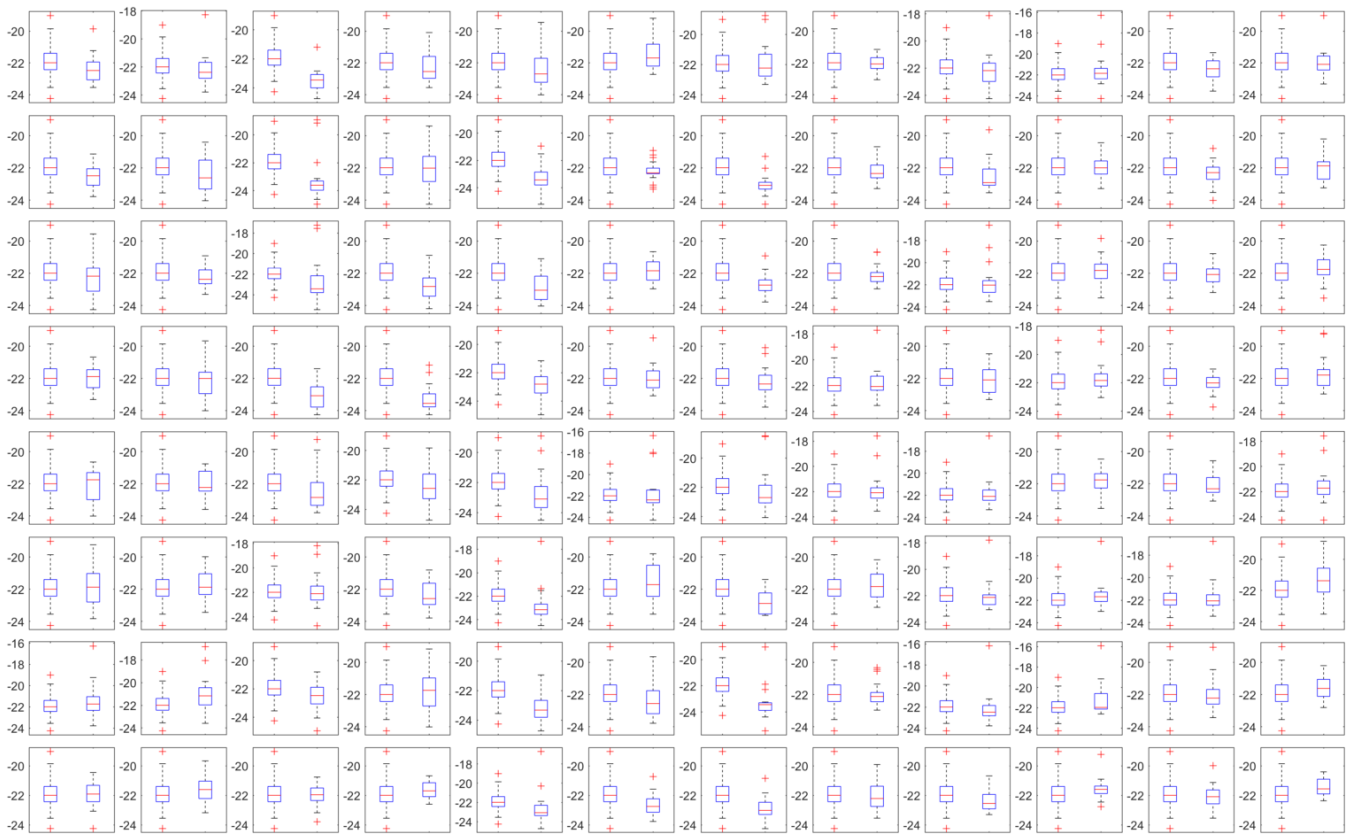
586 **HYSPLIT back trajectories**

587 The Hybrid Single-Particle Lagrangian Integrated Trajectory model (HYSPLIT) (Stein et al., 2015) was run using the
588 interactive web portal (Rolph et al., 2017). The trajectories were calculated using 0.5° resolution and the trajectories were
589 initialized 1000, 2000 and 3000 meters above the model terrain height. Although the majority of snow mass growth has been
590 shown to occur between mountaintop and 1 km above the surface (Lowenthal et al., 2016), these heights were chosen due to
591 the coarse resolution of the model terrain height and the observed sensitivity of the back trajectories with height. HYSPLIT
592 was initialized using the 0.5° hourly Global Data Assimilation System (GDAS) archived database and the vertical velocity was
593 model based rather than isentropic.



594

595 **Figure A1: Schematic of the 96-well tray holder from above (a) and the side (b), dimensions are in millimeters.**



596

597

598

599

600

Figure A2. A side by side comparison of box plots for the freezing temperatures of the 20 SA water experiments of the reference wells (left box) and the well represented by the location (right box) of each subplot. The median (red line), inter-quartile range (blue box), extreme values not considered outliers (whiskers) and outliers (red crosses) are shown as a function of temperature in °C (y-axes).

601

a. N=12



b. N=8



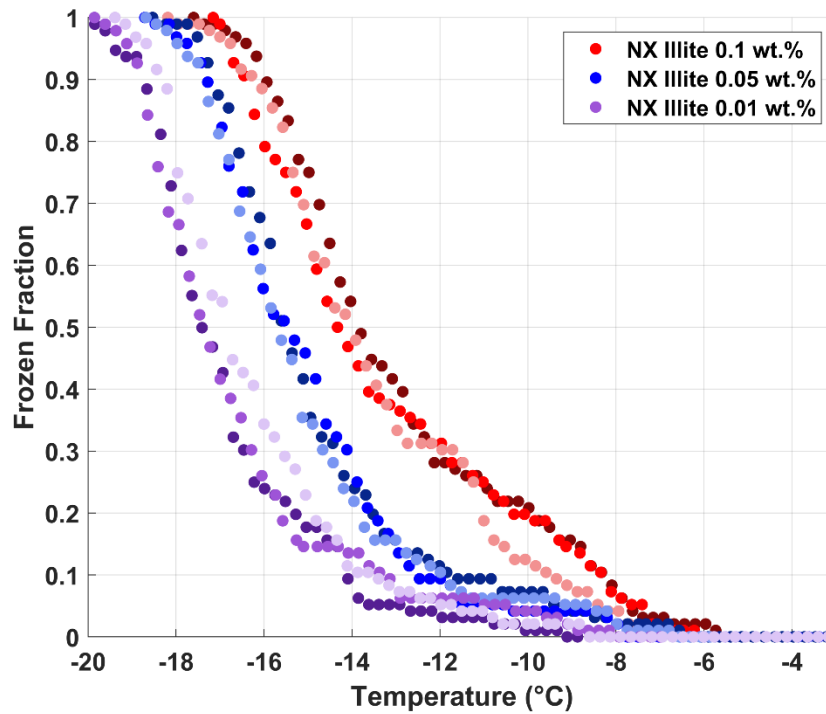
602

603 **Figure A3: (a) Bias in the freezing of SA water (°C) based on the median value of each well over 12 experiments and (b) 8 experiments**
 604 **relative to the median temperature of freezing for the 4 corner wells used during the temperature calibration. A positive (negative)**
 605 **bias indicates that the wells experience a warmer (colder) temperature than the four corner wells used for temperature calibration**
 606 **and therefore freeze at lower (higher) temperatures than reported.**

607

608

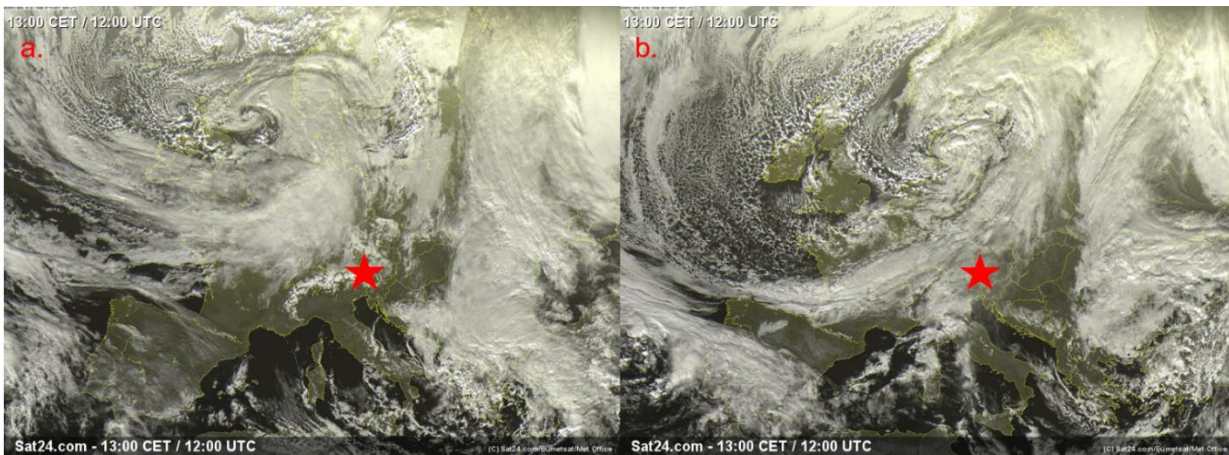
609



610

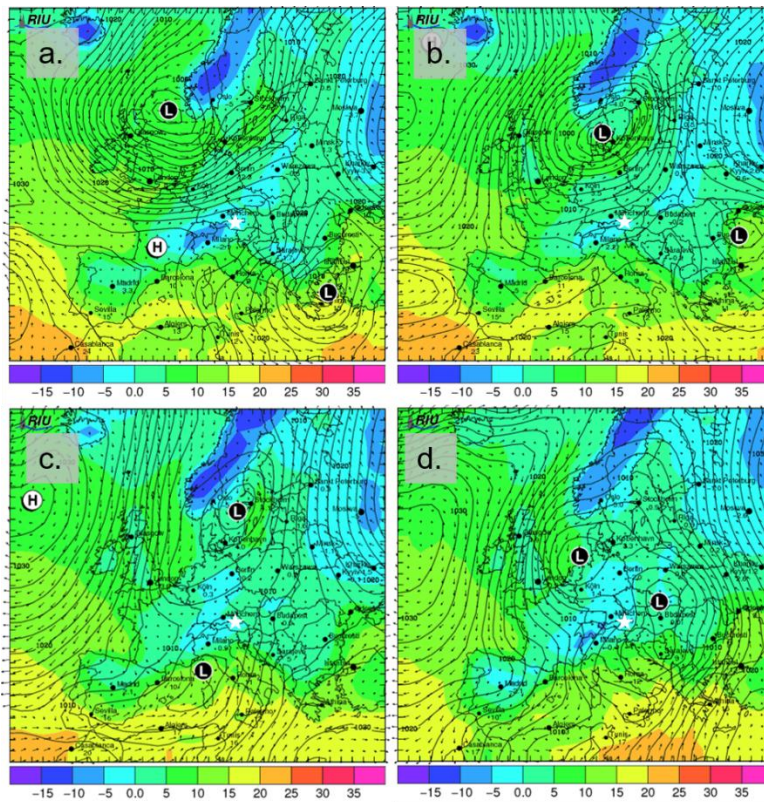
611 **Figure A4.** Frozen fraction curves of suspensions of 0.01 wt. % (magenta dots), 0.05 wt. % (red dots) and 0.01 wt. % (purple dots)
 612 of NX-illite run in triplicates as shown by shading.

613



614

615 **Figure A5:** Visible satellite image of the storm system impacting the SBO (red star) taken at 1200UTC on (a) Nov. 27th and (b) 28th.
 616 Images courtesy of Sat24.com/Eumetsat/Met Office (<http://www.sat24.com/history.aspx>).



617

618

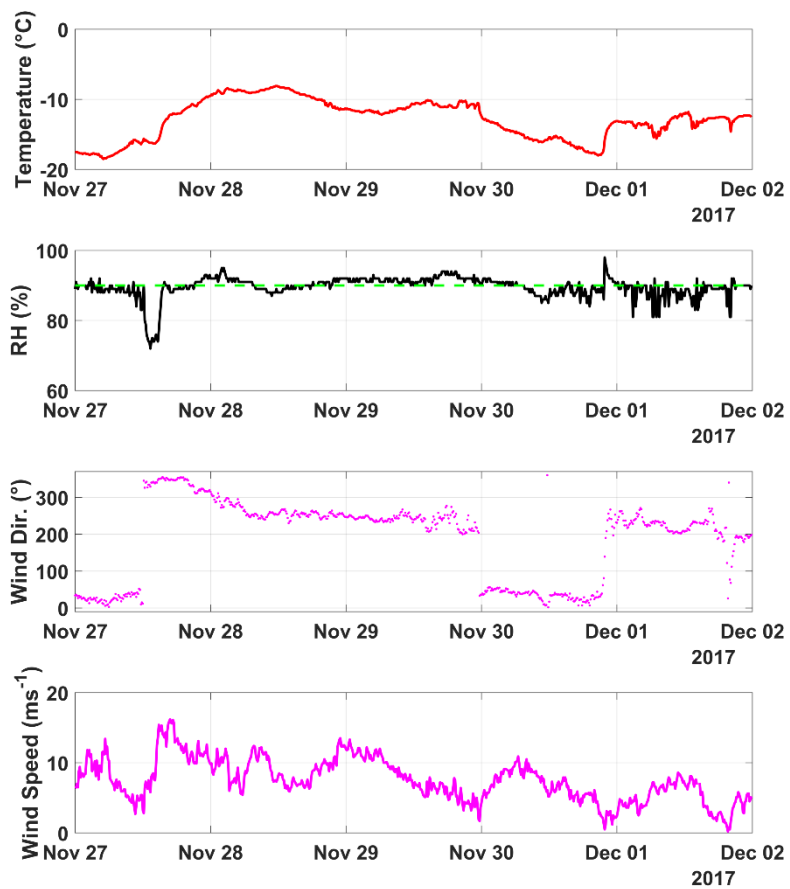
619

620

621

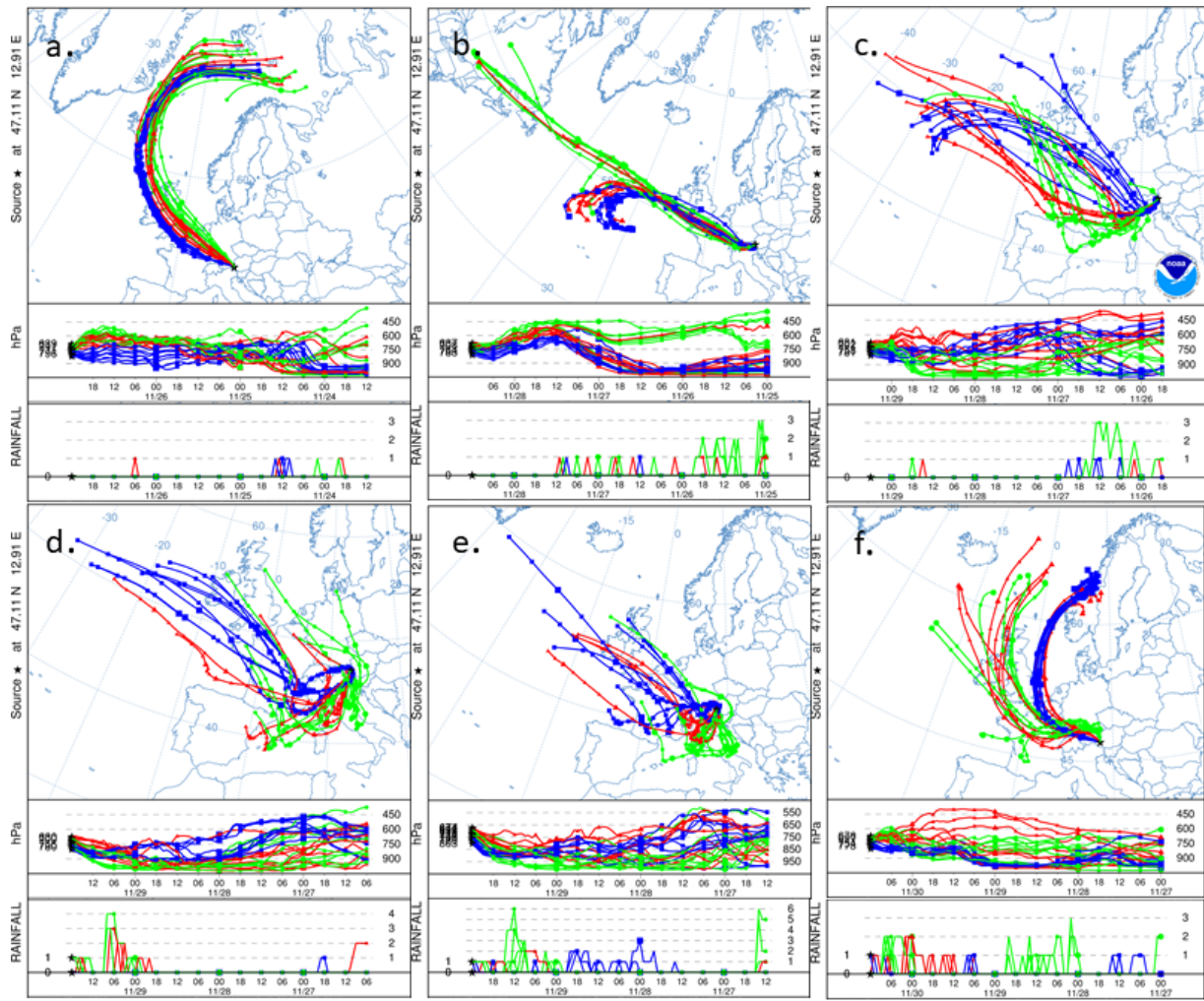
622

Figure A6: Forecasted surface pressure in hPa (black contours), 2 meter surface temperature in °C (color fill), and wind vectors in m/s (black arrows) for 12 UTC on (a) 27th, (b) 28th, (c) 29th and (d) 30th. Forecasts are based on model runs initialized on 00 UTC of the day of interest (12 hours before shown values). Surface low and high pressure centers are indicated with L and H, respectively. The location of SBO is shown by the white star. Images are taken and adapted from the Rhenish Institute for Environmental Research at the University of Cologne (http://www.uni-koeln.de/math-nat-fak/geommet/eurad/index_e.html).



624

625 **Figure A7: (top panel) Temperature (°C), (top-middle panel) humidity (%), (bottom-middle panel) wind direction (°) and (bottom**
 626 **panel) wind speed (ms⁻¹) as a function of date spanning from the 27th of November to the 2nd of December (in UTC). The humidity**
 627 **when cloud is present at SBO (90%) is shown (dashed green line).**



628

629

630

631

632

633

634

635

636

637

Figure A8: (a) 84-hour HYSPLIT back trajectories from the Sonnblick Observatory initialized on 00 UTC on the 27th, (b) 12 UTC on the 28th, (c) 06 UTC and (d) 18 UTC on the 29th, and (e) 00 UTC and (f) 12 UTC on the 30th of November. The blue, green and red lines represent 8 ensemble back trajectories initialized 1000 m, 2000 m and 3000 m above the model terrain height, respectively. The two lower panels in each subplot show the back trajectory height in units of pressure (hPa) and rainfall (mm) as a function of time (in 6 hourly intervals) as a function of pressure (in hPa).

638 **References**

- 639 Ansmann, A., Tesche, M., Seifert, P., Althausen, D., Engelmann, R., Fruntke, J., Wandinger, U., Mattis, I. and Müller, D.:
640 Evolution of the ice phase in tropical altocumulus: SAMUM lidar observations over Cape Verde, *J. Geophys. Res.*
641 *Atmospheres*, 114(D17), doi:10.1029/2008JD011659, 2009.
- 642 Atherton, T. J. and Kerbyson, D. J.: *Size Invariant Circle Detection.*, 1999.
- 643 Atkinson, J. D., Murray, B. J., Woodhouse, M. T., Whale, T. F., Baustian, K. J., Carslaw, K. S., Dobbie, S., O’Sullivan, D.
644 and Malkin, T. L.: The importance of feldspar for ice nucleation by mineral dust in mixed-phase clouds, *Nature*, 498(7454),
645 355, doi:10.1038/nature12278, 2013.
- 646 Ault, A. P., Williams, C. R., White, A. B., Neiman, P. J., Creamean, J. M., Gaston, C. J., Ralph, F. M. and Prather, K. A.:
647 Detection of Asian dust in California orographic precipitation, *J. Geophys. Res. Atmospheres*, 116(D16),
648 doi:10.1029/2010JD015351, 2011.
- 649 Beall, C. M., Stokes, M. D., Hill, T. C., DeMott, P. J., DeWald, J. T. and Prather, K. A.: Automation and heat transfer
650 characterization of immersion mode spectroscopy for analysis of ice nucleating particles, *Atmos Meas Tech*, 10(7), 2613–
651 2626, doi:10.5194/amt-10-2613-2017, 2017.
- 652 Beck, A., Henneberger, J., Fugal, J. P., David, R. O., Lacher, L. and Lohmann, U.: Impact of surface and near-surface processes
653 on ice crystal concentrations measured at mountain-top research stations, *Atmospheric Chem. Phys.*, 18(12), 8909–8927,
654 doi:https://doi.org/10.5194/acp-18-8909-2018, 2018.
- 655 Boer, G. de, Morrison, H., Shupe, M. D. and Hildner, R.: Evidence of liquid dependent ice nucleation in high-latitude stratiform
656 clouds from surface remote sensors, *Geophys. Res. Lett.*, 38(1), doi:10.1029/2010GL046016, 2011.
- 657 Boose, Y., Welti, A., Atkinson, J., Ramelli, F., Danielczok, A., Bingemer, H. G., Plötze, M., Sierau, B., Kanji, Z. A. and
658 Lohmann, U.: Heterogeneous ice nucleation on dust particles sourced from nine deserts worldwide – Part 1: Immersion
659 freezing, *Atmospheric Chem. Phys.*, 16(23), 15075–15095, doi:https://doi.org/10.5194/acp-16-15075-2016, 2016a.
- 660 Boose, Y., Kanji, Z. A., Kohn, M., Sierau, B., Zipori, A., Crawford, I., Lloyd, G., Bukowiecki, N., Herrmann, E., Kupiszewski,
661 P., Steinbacher, M. and Lohmann, U.: Ice Nucleating Particle Measurements at 241 K during Winter Months at 3580 m MSL
662 in the Swiss Alps, *J. Atmospheric Sci.*, 73(5), 2203–2228, doi:10.1175/JAS-D-15-0236.1, 2016b.
- 663 Broadley, S. L., Murray, B. J., Herbert, R. J., Atkinson, J. D., Dobbie, S., Malkin, T. L., Condliffe, E. and Neve, L.: Immersion
664 mode heterogeneous ice nucleation by an illite rich powder representative of atmospheric mineral dust, *Atmos Chem Phys*,
665 12(1), 287–307, doi:10.5194/acp-12-287-2012, 2012.
- 666 Burkert-Kohn, M., Wex, H., Welti, A., Hartmann, S., Grawe, S., Hellner, L., Herenz, P., Atkinson, J. D., Stratmann, F. and
667 Kanji, Z. A.: Leipzig Ice Nucleation chamber Comparison (LINC): intercomparison of four online ice nucleation counters,
668 *Atmos Chem Phys*, 17(18), 11683–11705, doi:10.5194/acp-17-11683-2017, 2017.
- 669 Christner, B. C., Cai, R., Morris, C. E., McCarter, K. S., Foreman, C. M., Skidmore, M. L., Montross, S. N. and Sands, D. C.:
670 Geographic, seasonal, and precipitation chemistry influence on the abundance and activity of biological ice nucleators in rain
671 and snow, *Proc. Natl. Acad. Sci.*, 105(48), 18854–18859, doi:10.1073/pnas.0809816105, 2008.
- 672 Creamean, J. M., Suski, K. J., Rosenfeld, D., Cazorla, A., DeMott, P. J., Sullivan, R. C., White, A. B., Ralph, F. M., Minnis,
673 P., Comstock, J. M., Tomlinson, J. M. and Prather, K. A.: Dust and Biological Aerosols from the Sahara and Asia Influence
674 Precipitation in the Western U.S., *Science*, 339(6127), 1572–1578, doi:10.1126/science.1227279, 2013.

- 675 Cziczko, D. J., Ladino, L., Boose, Y., Kanji, Z. A., Kupiszewski, P., Lance, S., Mertes, S. and Wex, H.: Measurements of Ice
676 Nucleating Particles and Ice Residuals, *Meteorol. Monogr.*, 58, 8.1-8.13, doi:10.1175/AMSMONOGRAPHS-D-16-0008.1,
677 2017.
- 678 DeMott, P. J., Cziczko, D. J., Prenni, A. J., Murphy, D. M., Kreidenweis, S. M., Thomson, D. S., Borys, R. and Rogers, D. C.:
679 Measurements of the concentration and composition of nuclei for cirrus formation, *Proc. Natl. Acad. Sci. U. S. A.*, 100(25),
680 14655–14660, doi:10.1073/pnas.2532677100, 2003.
- 681 DeMott, P. J., Prenni, A. J., McMeeking, G. R., Sullivan, R. C., Petters, M. D., Tobo, Y., Niemand, M., Möhler, O., Snider, J.
682 R., Wang, Z. and Kreidenweis, S. M.: Integrating laboratory and field data to quantify the immersion freezing ice nucleation
683 activity of mineral dust particles, *Atmospheric Chem. Phys.*, 15(1), 393–409, doi:10.5194/acp-15-393-2015, 2015.
- 684 DeMott, P. J., Hill, T. C. J., McCluskey, C. S., Prather, K. A., Collins, D. B., Sullivan, R. C., Ruppel, M. J., Mason, R. H.,
685 Irish, V. E., Lee, T., Hwang, C. Y., Rhee, T. S., Snider, J. R., McMeeking, G. R., Dhaniyala, S., Lewis, E. R., Wentzell, J. J.
686 B., Abbatt, J., Lee, C., Sultana, C. M., Ault, A. P., Axson, J. L., Martinez, M. D., Venero, I., Santos-Figueroa, G., Stokes, M.
687 D., Deane, G. B., Mayol-Bracero, O. L., Grassian, V. H., Bertram, T. H., Bertram, A. K., Moffett, B. F. and Franc, G. D.: Sea
688 spray aerosol as a unique source of ice nucleating particles, *Proc. Natl. Acad. Sci.*, 113(21), 5797–5803,
689 doi:10.1073/pnas.1514034112, 2016.
- 690 DeMott, P. J., Hill, T. C. J., Petters, M. D., Bertram, A. K., Tobo, Y., Mason, R. H., Suski, K. J., McCluskey, C. S., Levin, E.
691 J. T., Schill, G. P., Boose, Y., Rauker, A. M., Miller, A. J., Zaragoza, J., Rocci, K., Rothfuss, N. E., Taylor, H. P., Hader, J.
692 D., Chou, C., Huffman, J. A., Pöschl, U., Prenni, A. J. and Kreidenweis, S. M.: Comparative measurements of ambient
693 atmospheric concentrations of ice nucleating particles using multiple immersion freezing methods and a continuous flow
694 diffusion chamber, *Atmospheric Chem. Phys.*, 17(18), 11227–11245, doi:10.5194/acp-17-11227-2017, 2017.
- 695 Derrick, B. and White, P.: Why Welch’s test is Type I error robust, *Quant. Methods Psychol.*, 12, 30–38,
696 doi:10.20982/tqmp.12.1.p030, 2016.
- 697 Felgitsch, L., Baloh, P., Burkart, J., Mayr, M., Momken, M. E., Seifried, T. M., Winkler, P., Schmale III, D. G. and Grothe,
698 H.: Birch leaves and branches as a source of ice-nucleating macromolecules, *Atmospheric Chem. Phys.*, 18(21), 16063–16079,
699 doi:https://doi.org/10.5194/acp-18-16063-2018, 2018.
- 700 Field, P. R., Möhler, O., Connolly, P., Krämer, M., Cotton, R., Heymsfield, A. J., Saathoff, H. and Schnaiter, M.: Some ice
701 nucleation characteristics of Asian and Saharan desert dust, *Atmos Chem Phys*, 6(10), 2991–3006, doi:10.5194/acp-6-2991-
702 2006, 2006.
- 703 Fletcher, N. H.: *The physics of rainclouds*, Cambridge University Press., 1962.
- 704 Harrison, A. D., Whale, T. F., Rutledge, R., Lamb, S., Tarn, M. D., Porter, G. C. E., Adams, M. P., McQuaid, J. B., Morris,
705 G. J. and Murray, B. J.: An instrument for quantifying heterogeneous ice nucleation in multiwell plates using infrared emissions
706 to detect freezing, *Atmospheric Meas. Tech.*, 11(10), 5629–5641, doi:https://doi.org/10.5194/amt-11-5629-2018, 2018.
- 707 Hartmann, S., Niedermeier, D., Voigtländer, J., Clauss, T., Shaw, R. A., Wex, H., Kiselev, A. and Stratmann, F.: Homogeneous
708 and heterogeneous ice nucleation at LACIS: operating principle and theoretical studies, *Atmos Chem Phys*, 11(4), 1753–
709 1767, doi:10.5194/acp-11-1753-2011, 2011.
- 710 Hill, T. C. J., Moffett, B. F., DeMott, P. J., Georgakopoulos, D. G., Stump, W. L. and Franc, G. D.: Measurement of Ice
711 Nucleation-Active Bacteria on Plants and in Precipitation by Quantitative PCR, *Appl. Environ. Microbiol.*, 80(4), 1256–1267,
712 doi:10.1128/AEM.02967-13, 2014.

- 713 Hiranuma, N., Augustin-Bauditz, S., Bingemer, H., Budke, C., Curtius, J., Danielczok, A., Diehl, K., Dreischmeier, K., Ebert,
714 M., Frank, F., Hoffmann, N., Kandler, K., Kiselev, A., Koop, T., Leisner, T., Möhler, O., Nillius, B., Peckhaus, A., Rose, D.,
715 Weinbruch, S., Wex, H., Boose, Y., DeMott, P. J., Hader, J. D., Hill, T. C. J., Kanji, Z. A., Kulkarni, G., Levin, E. J. T.,
716 McCluskey, C. S., Murakami, M., Murray, B. J., Niedermeier, D., Petters, M. D., O'Sullivan, D., Saito, A., Schill, G. P., Tajiri,
717 T., Tolbert, M. A., Welti, A., Whale, T. F., Wright, T. P. and Yamashita, K.: A comprehensive laboratory study on the
718 immersion freezing behavior of illite NX particles: a comparison of 17 ice nucleation measurement techniques, *Atmos Chem*
719 *Phys*, 15(5), 2489–2518, doi:10.5194/acp-15-2489-2015, 2015.
- 720 Hiranuma, N., Adachi, K., Bell, D. M., Belosi, F., Beydoun, H., Bhaduri, B., Bingemer, H., Budke, C., Clemen, H.-C., Conen,
721 F., Cory, K. M., Curtius, J., DeMott, P. J., Eppers, O., Grawe, S., Hartmann, S., Hoffmann, N., Höhler, K., Jantsch, E., Kiselev,
722 A., Koop, T., Kulkarni, G., Mayer, A., Murakami, M., Murray, B. J., Nicosia, A., Petters, M. D., Piazza, M., Polen, M., Reicher,
723 N., Rudich, Y., Saito, A., Santachiara, G., Schiebel, T., Schill, G. P., Schneider, J., Segev, L., Stopelli, E., Sullivan, R. C.,
724 Suski, K., Szakáll, M., Tajiri, T., Taylor, H., Tobo, Y., Ullrich, R., Weber, D., Wex, H., Whale, T. F., Whiteside, C. L.,
725 Yamashita, K., Zelenyuk, A. and Möhler, O.: A comprehensive characterization of ice nucleation by three different types of
726 cellulose particles immersed in water, *Atmospheric Chem. Phys.*, 19(7), 4823–4849, doi:https://doi.org/10.5194/acp-19-4823-
727 2019, 2019.
- 728 Hoose, C. and Möhler, O.: Heterogeneous ice nucleation on atmospheric aerosols: a review of results from laboratory
729 experiments, *Atmos Chem Phys*, 12(20), 9817–9854, doi:10.5194/acp-12-9817-2012, 2012.
- 730 Irish, V. E., Elizondo, P., Chen, J., Chou, C., Charette, J., Lizotte, M., Ladino, L. A., Wilson, T. W., Gosselin, M., Murray, B.
731 J., Polishchuk, E., Abbatt, J. P. D., Miller, L. A. and Bertram, A. K.: Ice-nucleating particles in Canadian Arctic sea-surface
732 microlayer and bulk seawater, *Atmos Chem Phys*, 17(17), 10583–10595, doi:10.5194/acp-17-10583-2017, 2017.
- 733 Kanji, Z. A., Ladino, L. A., Wex, H., Boose, Y., Burkert-Kohn, M., Cziczo, D. J. and Krämer, M.: Overview of Ice Nucleating
734 Particles, *Meteorol. Monogr.*, 58, 1.1-1.33, doi:10.1175/AMSMONOGRAPHS-D-16-0006.1, 2017.
- 735 Kaufmann, L., Marcolli, C., Hofer, J., Pinti, V., Hoyle, C. R. and Peter, T.: Ice nucleation efficiency of natural dust samples
736 in the immersion mode, *Atmospheric Chem. Phys.*, 16(17), 11177–11206, doi:https://doi.org/10.5194/acp-16-11177-2016,
737 2016.
- 738 Kohn, M., Lohmann, U., Welti, A. and Kanji, Z. A.: Immersion mode ice nucleation measurements with the new Portable
739 Immersion Mode Cooling chamber (PIMCA), *J. Geophys. Res. Atmospheres*, 121(9), 4713–4733,
740 doi:10.1002/2016JD024761, 2016.
- 741 Lacher, L., Lohmann, U., Boose, Y., Zipori, A., Herrmann, E., Bukowiecki, N., Steinbacher, M. and Kanji, Z. A.: The
742 Horizontal Ice Nucleation Chamber (HINC): INP measurements at conditions relevant for mixed-phase clouds at the High
743 Altitude Research Station Jungfraujoch, *Atmospheric Chem. Phys.*, 17(24), 15199–15224, doi:https://doi.org/10.5194/acp-17-
744 15199-2017, 2017.
- 745 Lacher, L., Steinbacher, M., Bukowiecki, N., Herrmann, E., Zipori, A. and Kanji, Z. A.: Impact of Air Mass Conditions and
746 Aerosol Properties on Ice Nucleating Particle Concentrations at the High Altitude Research Station Jungfraujoch, *Atmosphere*,
747 9(9), 363, doi:10.3390/atmos9090363, 2018.
- 748 Lohmann, U. and Feichter, J.: Global indirect aerosol effects: a review, *Atmos Chem Phys*, 5(3), 715–737, doi:10.5194/acp-
749 5-715-2005, 2005.
- 750 Lowenthal, D., Hallar, A. G., McCubbin, I., David, R., Borys, R., Blossey, P., Muhlbauer, A., Kuang, Z. and Moore, M.:
751 Isotopic Fractionation in Wintertime Orographic Clouds, *J. Atmospheric Ocean. Technol.*, 33(12), 2663–2678,
752 doi:10.1175/JTECH-D-15-0233.1, 2016.

- 753 Lüönd, F., Stetzer, O., Welti, A. and Lohmann, U.: Experimental study on the ice nucleation ability of size-selected kaolinite
754 particles in the immersion mode, *J. Geophys. Res. Atmospheres*, 115(D14), doi:10.1029/2009JD012959, 2010.
- 755 Marcolli, C., Gedamke, S., Peter, T. and Zobrist, B.: Efficiency of immersion mode ice nucleation on surrogates of mineral
756 dust, *Atmos Chem Phys*, 7(19), 5081–5091, doi:10.5194/acp-7-5081-2007, 2007.
- 757 Matus, A. V. and L’Ecuyer, T. S.: The role of cloud phase in Earth’s radiation budget, *J. Geophys. Res. Atmospheres*, 122(5),
758 2559–2578, doi:10.1002/2016JD025951, 2017.
- 759 McCluskey, C. S., Ovadnevaite, J., Rinaldi, M., Atkinson, J., Belosi, F., Ceburnis, D., Marullo, S., Hill, T. C. J., Lohmann, U.,
760 Kanji, Z. A., O’Dowd, C., Kreidenweis, S. M. and DeMott, P. J.: Marine and Terrestrial Organic Ice-Nucleating Particles in
761 Pristine Marine to Continentally Influenced Northeast Atlantic Air Masses, *J. Geophys. Res. Atmospheres*, 123(11), 6196–
762 6212, doi:10.1029/2017JD028033, 2018.
- 763 Mühlmenstädt, J., Sourdeval, O., Delanoë, J. and Quaas, J.: Frequency of occurrence of rain from liquid-, mixed-, and ice-phase
764 clouds derived from A-Train satellite retrievals: RAIN FROM LIQUID- AND ICE-PHASE CLOUDS, *Geophys. Res. Lett.*,
765 42(15), 6502–6509, doi:10.1002/2015GL064604, 2015.
- 766 Murray, B. J., L. Broadley, S., W. Wilson, T., J. Bull, S., H. Wills, R., K. Christenson, H. and J. Murray, E.: Kinetics of the
767 homogeneous freezing of water, *Phys. Chem. Chem. Phys.*, 12(35), 10380–10387, doi:10.1039/C003297B, 2010.
- 768 Murray, B. J., O’Sullivan, D., D. Atkinson, J. and E. Webb, M.: Ice nucleation by particles immersed in supercooled cloud
769 droplets, *Chem. Soc. Rev.*, 41(19), 6519–6554, doi:10.1039/C2CS35200A, 2012.
- 770 Niemand, M., Möhler, O., Vogel, B., Vogel, H., Hoose, C., Connolly, P., Klein, H., Bingemer, H., DeMott, P., Skrotzki, J. and
771 Leisner, T.: A Particle-Surface-Area-Based Parameterization of Immersion Freezing on Desert Dust Particles, *J. Atmospheric
772 Sci.*, 69(10), 3077–3092, doi:10.1175/JAS-D-11-0249.1, 2012.
- 773 Petters, M. D. and Wright, T. P.: Revisiting ice nucleation from precipitation samples, *Geophys. Res. Lett.*, 42(20), 8758–
774 8766, doi:10.1002/2015GL065733, 2015.
- 775 Pinti, V., Marcolli, C., Zobrist, B., Hoyle, C. R. and Peter, T.: Ice nucleation efficiency of clay minerals in the immersion
776 mode, *Atmospheric Chem. Phys.*, 12(13), 5859–5878, doi:https://doi.org/10.5194/acp-12-5859-2012, 2012.
- 777 Polen, M., Brubaker, T., Somers, J. and Sullivan, R. C.: Cleaning up our water: reducing interferences from non-homogeneous
778 freezing of $\langle q \rangle$ pure </math> water in droplet freezing assays of ice nucleating particles, *Atmospheric Meas. Tech. Discuss.*, 1–31,
779 doi:https://doi.org/10.5194/amt-2018-134, 2018.
- 780 Pummer, B. G., Bauer, H., Bernardi, J., Bleicher, S. and Grothe, H.: Suspendable macromolecules are responsible for ice
781 nucleation activity of birch and conifer pollen, *Atmos Chem Phys*, 12(5), 2541–2550, doi:10.5194/acp-12-2541-2012, 2012.
- 782 Puxbaum, H. and Tschewenka, W.: Relationships of major ions in snow fall and rime at sonnblick observatory (SBO, 3106m)
783 and implications for scavenging processes in mixed clouds, *Atmos. Environ.*, 32(23), 4011–4020, doi:10.1016/S1352-
784 2310(98)00244-1, 1998.
- 785 Reicher, N., Segev, L. and Rudich, Y.: The Weizmann Supercooled Droplets Observation on a Microarray (WISDOM) and
786 application for ambient dust, *Atmos Meas Tech*, 11(1), 233–248, doi:10.5194/amt-11-233-2018, 2018.
- 787 Richardson, M. S., DeMott, P. J., Kreidenweis, S. M., Cziczo, D. J., Dunlea, E. J., Jimenez, J. L., Thomson, D. S., Ashbaugh,
788 L. L., Borys, R. D., Westphal, D. L., Casuccio, G. S. and Lersch, T. L.: Measurements of heterogeneous ice nuclei in the

- 789 western United States in springtime and their relation to aerosol characteristics, *J. Geophys. Res. Atmospheres*, 112(D2),
790 D02209, doi:10.1029/2006JD007500, 2007.
- 791 Riechers, B., Wittbracht, F., H[?]tten, A. and Koop, T.: The homogeneous ice nucleation rate of water droplets produced in a
792 microfluidic device and the role of temperature uncertainty, *Phys. Chem. Chem. Phys.*, 15(16), 5873, doi:10.1039/c3cp42437e,
793 2013.
- 794 Roebber, P. J., Bruening, S. L., Schultz, D. M. and Cortinas, J. V.: Improving Snowfall Forecasting by Diagnosing Snow
795 Density, *Weather Forecast.*, 18(2), 264–287, doi:10.1175/1520-0434(2003)018<0264:ISFBDS>2.0.CO;2, 2003.
- 796 Rogers, D. C.: Development of a continuous flow thermal gradient diffusion chamber for ice nucleation studies, *Atmospheric*
797 *Res.*, 22(2), 149–181, doi:10.1016/0169-8095(88)90005-1, 1988.
- 798 Rolph, G., Stein, A. and Stunder, B.: Real-time Environmental Applications and Display sYstem: READY, *Environ. Model.*
799 *Softw.*, 95, 210–228, doi:10.1016/j.envsoft.2017.06.025, 2017.
- 800 Spiess, A.-N., Feig, C. and Ritz, C.: Highly accurate sigmoidal fitting of real-time PCR data by introducing a parameter for
801 asymmetry, *BMC Bioinformatics*, 9, 221, doi:10.1186/1471-2105-9-221, 2008.
- 802 Stan, C. A., Schneider, G. F., Shevkopyas, S. S., Hashimoto, M., Ibanescu, M., Wiley, B. J. and Whitesides, G. M.: A
803 microfluidic apparatus for the study of ice nucleation in supercooled water drops, *Lab. Chip*, 9(16), 2293–2305,
804 doi:10.1039/B906198C, 2009.
- 805 Stein, A. F., Draxler, R. R., Rolph, G. D., Stunder, B. J. B., Cohen, M. D. and Ngan, F.: NOAA’s HYSPLIT Atmospheric
806 Transport and Dispersion Modeling System, *Bull. Am. Meteorol. Soc.*, 96(12), 2059–2077, doi:10.1175/BAMS-D-14-
807 00110.1, 2015.
- 808 Stetzer, O., Baschek, B., Lüönd, F. and Lohmann, U.: The Zurich Ice Nucleation Chamber (ZINC)-A New Instrument to
809 Investigate Atmospheric Ice Formation, *Aerosol Sci. Technol.*, 42(1), 64–74, doi:10.1080/02786820701787944, 2008.
- 810 Stopelli, E., Conen, F., Zimmermann, L., Alewell, C. and Morris, C. E.: Freezing nucleation apparatus puts new slant on study
811 of biological ice nucleators in precipitation, *Atmospheric Meas. Tech.*, 7(1), 129–134, doi:10.5194/amt-7-129-2014, 2014.
- 812 Stopelli, E., Conen, F., Morris, C. E., Herrmann, E., Bukowiecki, N. and Alewell, C.: Ice nucleation active particles are
813 efficiently removed by precipitating clouds, *Sci. Rep.*, 5, 16433, doi:10.1038/srep16433, 2015.
- 814 Tan, I., Storelvmo, T. and Zelinka, M. D.: Observational constraints on mixed-phase clouds imply higher climate sensitivity,
815 *Science*, 352(6282), 224–227, doi:10.1126/science.aad5300, 2016.
- 816 Tarn, M. D., Sikora, S. N. F., Porter, G. C. E., O’Sullivan, D., Adams, M., Whale, T. F., Harrison, A. D., Vergara-Temprado,
817 J., Wilson, T. W., Shim, J. and Murray, B. J.: The study of atmospheric ice-nucleating particles via microfluidically generated
818 droplets, *Microfluid. Nanofluidics*, 22(5), doi:10.1007/s10404-018-2069-x, 2018.
- 819 Vali, G.: Quantitative Evaluation of Experimental Results an the Heterogeneous Freezing Nucleation of Supercooled Liquids,
820 *J. Atmospheric Sci.*, 28(3), 402–409, doi:10.1175/1520-0469(1971)028<0402:QEOERA>2.0.CO;2, 1971.
- 821 Vali, G.: Revisiting the differential freezing nucleus spectra derived from drop-freezing experiments: methods of calculation,
822 applications, and confidence limits, *Atmospheric Meas. Tech.*, 12(2), 1219–1231, doi:https://doi.org/10.5194/amt-12-1219-
823 2019, 2019.

- 824 Vali, G. and Upper, C. D.: Principles of Ice Nucleation, in *Biological Ice Nucleation and Its Applications*, edited by R. E. Lee,
825 G. J. Warren, and L. V. Gusta, p. 370, The American Phytopathological Society, St. Paul, Minnesota, USA. [online] Available
826 from: <https://www.loot.co.za/product/richard-e-lee-biological-ice-nucleation-and-its-applica/wxrm-421-gaa0> (Accessed 16
827 September 2019), 1995.
- 828 Vali, G., DeMott, P. J., Möhler, O. and Whale, T. F.: Technical Note: A proposal for ice nucleation terminology, *Atmospheric*
829 *Chem. Phys.*, 15(18), 10263–10270, doi:10.5194/acp-15-10263-2015, 2015.
- 830 Welti, A., Müller, K., Fleming, Z. L. and Stratmann, F.: Concentration and variability of ice nuclei in the subtropical maritime
831 boundary layer, *Atmos Chem Phys*, 18(8), 5307–5320, doi:10.5194/acp-18-5307-2018, 2018.
- 832 Westbrook, C. D. and Illingworth, A. J.: Evidence that ice forms primarily in supercooled liquid clouds at temperatures >
833 -27°C , *Geophys. Res. Lett.*, 38(14), doi:10.1029/2011GL048021, 2011.
- 834 Wex, H., Augustin-Bauditz, S., Boose, Y., Budke, C., Curtius, J., Diehl, K., Dreyer, A., Frank, F., Hartmann, S., Hiranuma,
835 N., Jantsch, E., Kanji, Z. A., Kiselev, A., Koop, T., Möhler, O., Niedermeier, D., Nillius, B., Rösch, M., Rose, D., Schmidt,
836 C., Steinke, I. and Stratmann, F.: Intercomparing different devices for the investigation of ice nucleating particles using
837 Snomax<sup><sup></sup></sup> as test substance, *Atmospheric Chem. Phys.*, 15(3), 1463–1485, doi:10.5194/acp-15-1463-
838 2015, 2015.
- 839 Wex, H., Huang, L., Zhang, W., Hung, H., Traversi, R., Becagli, S., Sheesley, R. J., Moffett, C. E., Barrett, T. E., Bossi, R.,
840 Skov, H., Hünerbein, A., Lubitz, J., Löffler, M., Linke, O., Hartmann, M., Herenz, P. and Stratmann, F.: Annual variability of
841 ice-nucleating particle concentrations at different Arctic locations, *Atmospheric Chem. Phys.*, 19(7), 5293–5311,
842 doi:<https://doi.org/10.5194/acp-19-5293-2019>, 2019.
- 843 Whale, T. F., Murray, B. J., O'Sullivan, D., Wilson, T. W., Umo, N. S., Baustian, K. J., Atkinson, J. D., Workneh,
844 D. A. and Morris, G. J.: A technique for quantifying heterogeneous ice nucleation in microlitre supercooled water droplets,
845 *Atmospheric Meas. Tech.*, 8(6), 2437–2447, doi:10.5194/amt-8-2437-2015, 2015.
- 846 Wilson, T. W., Ladino, L. A., Alpert, P. A., Breckels, M. N., Brooks, I. M., Browse, J., Burrows, S. M., Carslaw, K. S.,
847 Huffman, J. A., Judd, C., Kilthau, W. P., Mason, R. H., McFiggans, G., Miller, L. A., Nájera, J. J., Polishchuk, E., Rae, S.,
848 Schiller, C. L., Si, M., Temprado, J. V., Whale, T. F., Wong, J. P. S., Wurl, O., Yakobi-Hancock, J. D., Abbatt, J. P. D., Aller,
849 J. Y., Bertram, A. K., Knopf, D. A. and Murray, B. J.: A marine biogenic source of atmospheric ice-nucleating particles,
850 *Nature*, 525(7568), 234, doi:10.1038/nature14986, 2015.

851